Electronic Supplementary Material (ESI) for ChemComm.
This journal is © The Royal Society of Chemistry 2018

Electronic Supporting Information

Ni-porphyrin based small molecules for efficient organic solar cells (>9.0 %) with high open circuit voltage of over 1.0 V and low energy loss

Maida Vartanian,[a] Rahul Singhal,[b] Pilar de la Cruz,[a] Ganesh D. Sharma,[c,*] and Fernando Langa.[a,*]

[a]Universidad de Castilla-La Mancha. Institute of Nanoscience, Nanotechnology and Molecular Materials (INAMOL), Campus de la Fábrica de Armas, Toledo. Spain. Tel: 34 9252 68843. E-mail: Fernando.Langa@uclm.es

[b]Department of Physics, Malviya National Institute of Technology (MNIT), Jaipur

[c]Department of Physics, The LNM Institute of Information Technology (Deemed University), Rupa ki Nangal, Jamdoli, Jaipur (Raj.) 302031, India E-mail: gdharma273@gmail.com

1. Experimental Conditions.

All solvents and reagents were purchased from Aldrich Chemicals. The solvents were used without previous purification. Anhydrous solvents were dried by purification system Pure-Sov 400. Chromatographic purifications were performed using silica gel 60 Merk 70-230 mesh ASTM. Gel Permeation Chromatograpy (GPC) column was performed using Bio-Beads ® S-X1 Beads 200-400 Mesh as stationary phase. Analytical thin-layer chromatography was performed using ALUGRAM ® SIL G/UV_{254} silica gel 60. Nuclear magnetic resonance ^{1}H-NMR and ^{13}C-NMR were performed using Bruker Innova 400 Hz. Chemical shifts (δ) values are denoted in ppm. Residual solvent peaks being used as the internal standard ($CHCl_3$; δ = 7.27 ppm). ^{13}C NMR chemical shifts are reported relative to the solvent residual peaks ($CDCl_3$, δ = 77.36 ppm). MALDI-TOF spectra were obtained in VOYAGER DETM STR spectrometry, using dithranol [1,8-dihydroxy-9(10H)-anthracenone] as matrix. Fourier transform infrared spectrophotometer (FT-IR) Thermo Nicolet AVATAR 370 was used with ATR (Attenuated Total Reflection) method or using KBr pellet, in each case the most characteristic bands are indicated for each compound. Absorption spectra were performed on Shimadzu UV 3600 spectrophotometer. Solutions of different concentration were prepared in CH_2Cl_2, spectroscopy grade, with absorbance between 0.2 and 0.3 using a 1 cm UV cuvette. Film thickness for UV-Vis were deposited by spin-coating (60 s, 3000 rpm) on cover slips (22x22 mm) from solutions of **MV143** in $CHCl_3$ (10^{-4}M). The thermal stability was evaluated by TGA on a Mettler Toledo TGA/DSC Start^{e} System under nitrogen, with a heating rate of 10 ºC/min.

Electrochemical Measurements: Reduction (E_{red}) and oxidation potentials (E_{ox}) were measured by cyclic voltammetry with a potentiostat BAS CV50W in a conventional three-electrode cell equipped with a glassy carbon working electrode, a platinum wire counter electrode, and an $Ag/AgNO_3$ reference electrode at scan rate of 100 mV/s. The E_{red} and E_{ox} were expressed vs. Fc/Fc^{+} used as external reference. In each case, the measurements were done in a deaerated solution containing 1 mM of a the sample compound in 0.1 M of (n-Bu)$_4$NClO$_4$ in *o*-DCB:Acetonitrile (4:1) as an electrolyte solution.

Computational Details: Theoretical calculations were carried out within the density functional theory (DFT) framework by using the Gaussian 09,[1] applying density functional theory at the B3LYP level. The basis set of 6-31G* was used in the calculations (Supercomputation Service of UCLM).

Device fabrication and characterization: OSCs with a conventional configuration (ITO/PEDOT:PSS/**MV143**:$PC_{71}BM$/PFN/Al) were fabricated as follows: The indium tin oxide coated glass substrate was cleaned ultrasonically with deionized water, acetone, and isopropanol sequentially for 10 min each. The organic residues were removed by treatment with UV-ozone for 1 h. A thin layer of PEDOT:PSS (35 nm) was spin coated on the top of ITO glass and dried at 110ºC for 15 min. The active layer consisting of **MV143**:$PC_{71}BM$ (16 mg/mL in CB and the corresponding donor to acceptor weight ratios) was spin coated on the top of PEDOT:PSS/ITO and dried under ambient conditions at room temperature. For the solvent vapour annealing the active layers were placed in a petri dish containing carbon disulfide CS_2 for 40 s and then removed. A methanol solution of PFN with a concentration of 1.5 mg/mL was then spin-coated on top of the active layer at 3000 rpm for 30 s. The thickness of the active layers was 85±5 nm. Finally, an Al top electrode was deposited onto the top of the PFN buffer layer by thermal evaporation at a base pressure of 2.0×10^{-5} Pa. The effective area of the devices was around 16 mm^2.

The hole-only and electron-only devices with ITO/PEDOT:PSS/active layer/Au and ITO/Al/active layer/Al architectures were also fabricated in a similar way in order to measure the hole and electron mobilities, respectively. The current–voltage (*J*-*V*) characteristics of the BHJ organic solar cells were measured using a computer-controlled

[1] Gaussian 09, Revision A.02, M. J. Frisch, G. W. Trucks, H. B. Schlegel, G. E. Scuseria, M. A. Robb, J. R. Cheeseman, G. Scalmani, V. Barone, G. A. Petersson, H. Nakatsuji, X. Li, M. Caricato, A. Marenich, J. Bloino, B. G. Janesko, R. Gomperts, B. Mennucci, H. P. Hratchian, J. V. Ortiz, A. F. Izmaylov, J. L. Sonnenberg, D. Williams-Young, F. Ding, F. Lipparini, F. Egidi, J. Goings, B. Peng, A. Petrone, T. Henderson, D. Ranasinghe, V. G. Zakrzewski, J. Gao, N. Rega, G. Zheng, W. Liang, M. Hada, M. Ehara, K. Toyota, R. Fukuda, J. Hasegawa, M. Ishida, T. Nakajima, Y. Honda, O. Kitao, H. Nakai, T. Vreven, K. Throssell, J. A. Montgomery, Jr., J. E. Peralta, F. Ogliaro, M. Bearpark, J. J. Heyd, E. Brothers, K. N. Kudin, V. N. Staroverov, T. Keith, R. Kobayashi, J. Normand, K. Raghavachari, A. Rendell, J. C. Burant, S. S. Iyengar, J. Tomasi, M. Cossi, J. M. Millam, M. Klene, C. Adamo, R. Cammi, J. W. Ochterski, R. L. Martin, K. Morokuma, O. Farkas, J. B. Foresman, and D. J. Fox, Gaussian, Inc., Wallingford CT, 2016.

Keithley 2400 source meter in the dark and under a simulated AM 1.5G illumination of 100 mW/cm^2. A xenon light source coupled with an optical filter was used to provide the stimulated irradiance at the surface of the devices. The incident photon to current efficiency (IPCE) of the devices was measured by illuminating the device through the light source and the monochromator and the resulting current was measured using a Keithley electrometer under short circuit conditions.

2. Synthetic procedures

Compound 2. Under an Ar atmosphere, in a two-necked 1 L round-bottomed flask, porphyrin **1** (406 mg, 0.74 mmol) was dissolved in HPLC grade toluene (120 mL). Nickel(II) acetylacetonate (1.9 g, 7.4 mmol, 10 eq) was added and the reaction mixture was vigorously stirred overnight at 112ºC. The solvent was removed under reduced pressure. The resulting crude mixture was filtered through a silica pad (hexane/$CHCl_3$ 3:2) to give a quantitative yield of **2** as a dark red solid. ^{1}H-NMR (400 MHz, $CDCl_3$) δ/ppm: 9.92 (s, 2H), 9.17 (d, *J* = 4.7 Hz, 4H), 8.80 (d, *J* = 4.7 Hz, 4H), 7.27 (s, 4H), 2.63 (s, 6H), 1.80 (s, 12H); ^{13}C-NMR (100 MHz, $CDCl_3$) δ/ppm: 143.1, 143.0, 139.5, 138.1, 137.7, 132.7, 131.6, 128.1, 117.1, 105.1, 21.8, 21.7; FT-IR (ATR) ν/cm^{-1}: 1458, 1323, 1063, 992, 846, 784, 690; MS-MALDI TOF (m/z): found 602.35 $[M]^+$; calcd for $C_{38}H_{32}N_4Ni$: 602.20; UV/vis (CH_2Cl_2) λ/nm (log ε): 402 (5.34), 516 (4.20), 550 (3.44).

Compound 3. In a three-necked 500 mL round-bottomed flask, compound **2** (217 mg, 0.36 mmol) was dissolved in HPLC grade $CHCl_3$ (200 mL). Ar was bubbled through the solution and the reaction mixture was cooled to 0ºC. Pyridine (1 mL) was added. NBS (120 mg, 0.72 mmol, 2 eq) was dissolved in $CHCl_3$ (30 mL) and the solution was added dropwise to the reaction mixture. The mixture was stirred overnight, during which time it warmed up to room temperature. The solvent was removed under reduced pressure. The crude mixture was filtered through a silica pad (hexane/$CHCl_3$ 3:2) to give a quantitative yield of **3** as a dark purple solid. ^{1}H-NMR (400 MHz, $CDCl_3$) δ/ppm: 9.45 (d, *J* = 4.9 Hz, 4H), 8.60 (d, *J* = 4.9 Hz, 4H), 7.24 (s, 4H), 2.60 (s, 6H), 1.81 (s, 12H); ^{13}C-NMR (100 MHz, $CDCl_3$) δ/ppm: 143.5, 143.2, 139.2, 138.4, 136.7, 134.2, 133.0, 128.2, 118.9, 102.9, 21.74, 21.7; FT-IR (KBr) ν/cm^{-1}: 3440, 2916, 2854, 1458, 1311, 1003, 795; MS-MALDI TOF (m/z): found 760.24 $[M]^+$; calcd for $C_{38}H_{30}Br_2N_4Ni$: 760.02; UV/vis (CH_2Cl_2) λ/nm (log ε): 418 (5.33), 536 (4.22).

Compound 4. In a 100 mL Schlenk flask, $Pd(PPh_3)_2Cl_2$ (31 mg, 0.04 mmol, 0.12 eq), CuI (3.5 mg, 0.02 mmol, 0.05 eq) were charged and kept under vacuum for 0.5 h. Three purge cycles of Ar/vacuum were performed. A solution of compound **3** (277 mg, 0.36 mmol) in THF (55 mL) was introduced into the flask by syringe. Ethynyltrimethylsilane (2 mL, 14 mmol, 40 eq) and NEt_3 (12 mL) were added. The reaction mixture was stirred overnight at room temperature. The solvents were removed under reduced pressure. The crude product was loaded onto a silica column (hexane/$CHCl_3$ 0.9:0.1 to 1:2) and purified to give **4** (262 mg, 91%) as a purple solid. ^{1}H-NMR (400 MHz, $CDCl_3$) δ/ppm: 9.44 (d, *J* = 4.8 Hz, 4H), 8.57(d, *J* = 4.8 Hz, 4H), 7.23 (s, 4H), 2.60 (s, 6H), 1.80 (s, 12H), 0.53 (s, 18H); ^{13}C-NMR (100 MHz, $CDCl_3$) δ/ppm: 145.3, 143.2, 139.2, 138.2, 137.0, 132.4, 132.1, 128.1, 119.3, 105.3, 102.9, 100.2, 21.8, 21.6, 0.6; FT-IR (ATR) ν/cm^{-1}: 2916, 2854, 1003, 841, 756, 702; MS-MALDI TOF (m/z): found 794.45 $[M]^+$; calcd for $C_{48}H_{48}N_4NiSi_2$: 794.30); UV/vis (CH_2Cl_2) λ/nm (log ε): 434 (5.30), 552 (4.00), 590 (4.22).

Compound 5. In a 100 mL round-bottomed flask, compound **4** (123 mg, 0.16 mmol) was dissolved in CH_2Cl_2 (33 mL) and kept under argon. TBAF (1 M, 0.7 mL, 4.5 eq) was added and the reaction mixture was stirred at r.t. for 35 min. $CaCl_2$ (500 mg, 4.5 mmol, 30 eq) was added and the mixture was stirred for an additional 5 min. Extractions were performed (H_2O/CH_2Cl_2) and the organic phase was dried over Na_2SO_4, filtered and concentrated to give a red solid, which was used directly in the next step. MS-MALDI TOF (m/z): found 650.27 $[M]^+$; calcd for $C_{42}H_{32}N_4Ni$: 650.20.

Compound 7. In a 100 mL Schlenk flask, $Pd_2(dba)_3$ (125 mg, 0.14 mmol, 0.9 eq), $AsPh_3$ (245 mg, 0.83 mmol, 5.2 eq) were charged and kept under vacuum for 0.5 h. Three purge cycles of Ar/vacuum were performed. A solution of porphyrin **5** (101 mg, 0.16 mmol) in toluene (30 mL) was introduced into the flask by syringe. A solution of compound **6** (460 mg, 0.67 mmol, 4.2 eq) in toluene (10 mL) and NEt_3 (7 mL) were added. The reaction mixture was stirred overnight at 86°C. Heating was stopped and the mixture was filtered through a Celite® pad. The filtrates were concentrated and filtered through silica ($CHCl_3$), followed by GPC (CH_2Cl_2), column chromatography (silica, 1:1 $CHCl_3$/Hexane), GPC (CH_2Cl_2), filtration (silica, $CHCl_3$) and precipitation from MeOH (×3). Compound **7** (150 mg, 55%) was obtained as a shiny dark green solid. ^{1}H-NMR (400 MHz, $CDCl_3$) δ/ppm: 10.01 (s, 2H), 9.43 (d, *J* = 4.8 Hz, 4H), 8.58 (d, *J* = 4.8 Hz, 4H), 7.35 (d, *J* = 15.5 Hz, 2H), 7.25 (s, 4H), 7.10 (d, *J* = 15.5 Hz, 2H), 3.02 (t, *J* = 8 Hz, 4H), 2.88 (t, *J* = 8 Hz, 4H), 2.73 (t, *J* = 8 Hz, 4H), 2.67 (t, *J* = 8 Hz, 4H), 2.61 (s, 6H),

1.93–1.85 (m, 16H), 1.63–1.26 (m, 50H), 0.97–0.90 (m, 18H), 0.80 (t, *J* = 7.2 Hz, 6H); ^{13}C-NMR (100 MHz, $CDCl_3$) δ/ppm: 182.3, 153.4, 149.3, 147.0, 144.8, 143.0, 142.9, 142.5, 139.2, 138.3, 138.0, 136.9, 135.3, 132.2, 131.9, 128.2, 123.7, 119.8, 119.6, 118.8, 100.7, 98.6, 91.8, 32.6, 32.1, 32.1, 32.0, 31.9, 31.8, 31.6, 31.2, 30.0, 29.8, 29.7, 29.6, 27.8, 27.5, 26.8, 23.0, 22.9, 21.8, 21.6, 14.5, 14.5, 14.4, 14.3; FT-IR (ATR) ν/cm^{-1}: 2924, 2854, 1651, 1458, 1242, 1003, 795; MS-MALDI TOF (m/z): found 1761.56 $[M]^+$; calcd for $C_{112}H_{140}N_4NiO_2S_4$: 1760.92; UV/vis ($CH_2Cl_2$) λ/nm (log ε): 494 (5.28), 662 (4.89).

Synthesis of MV143. In a 100 mL round-bottomed flask compound **7** (83 mg, 0.05 mmol) was dissolved in $CHCl_3$ (15 mL) and 3-ethylrhodanine (450 mg, 2.79 mmol, 55 eq) was added. Ar was bubbled through the mixture and then piperidine (0.3 mL) was added. The reaction mixture was stirred overnight at 62 °C. The solvent was removed under reduced pressure. The crude material was filtered through a silica pad ($CHCl_3$), followed by GPC (CH_2Cl_2), refiltration through silica ($CHCl_3$) and then precipitation from *n*-pentane and then MeOH. **MV143** (65mg, 67%) was obtained as a shiny green solid. ^{1}H-NMR (400 MHz, $CDCl_3$) δ/ppm: 9.43 (d, *J* = 4.8 Hz, 4H), 8.57 (d, *J* = 4.8 Hz, 4H), 7.95 (s, 2H), 7.29 (d, *J* = 15.6 Hz, 2H), 7.25 (s, 4H), 7.14 (d, *J* = 15.6 Hz, 2H), 4.23 (q, *J* = 7 Hz, 4H), 3.04 (t, *J* = 4 Hz, 4H), 2.81–2.67 (m, 12H), 2.61 (s, 6H), 1.91–1.85 (m, 16H), 1.70–1.28 (m, 54H), 0.97–0.91 (m, 18H), 0.80 (t, *J* = 7.2 Hz, 6H); ^{13}C-NMR (100 MHz, $CDCl_3$) δ/ppm: 192.8, 167.9, 151.1, 149.5, 145.6, 144.8, 142.9, 142.8, 142.7, 139.2, 138.4, 138.3, 136.9, 132.2, 132.0, 131.1, 128.2, 124.2, 122.6, 119.8, 119.5, 118.6, 100.70, 91.9, 40.3, 32.1, 32.1, 32.0, 31.9, 31.8, 31.7, 31.5, 31.2, 30.1, 30.0, 29.7, 29.6, 29.5, 28.0, 27.7, 27.5, 23.0, 22.9, 21.8, 21.6, 14.6, 14.5, 14.4, 14.3, 12.7; FT-IR (ATR) ν/cm^{-1}: 2926, 2856, 1705, 1566, 1319, 1226, 1126, 1002, 793; MS-MALDI TOF (m/z): found 2047.05 $[M]^+$; calcd for $C_{122}H_{150}N_6NiO_2S_8$: 2046.90); UV/vis ($CH_2Cl_2$) λ/nm (log ε): 682 (5.1), 540 (5.1), 350 (4.7).

3. ^{1}H-NMR, ^{13}C-NMR, FT-IR and MALDI-TOF MS spectra.

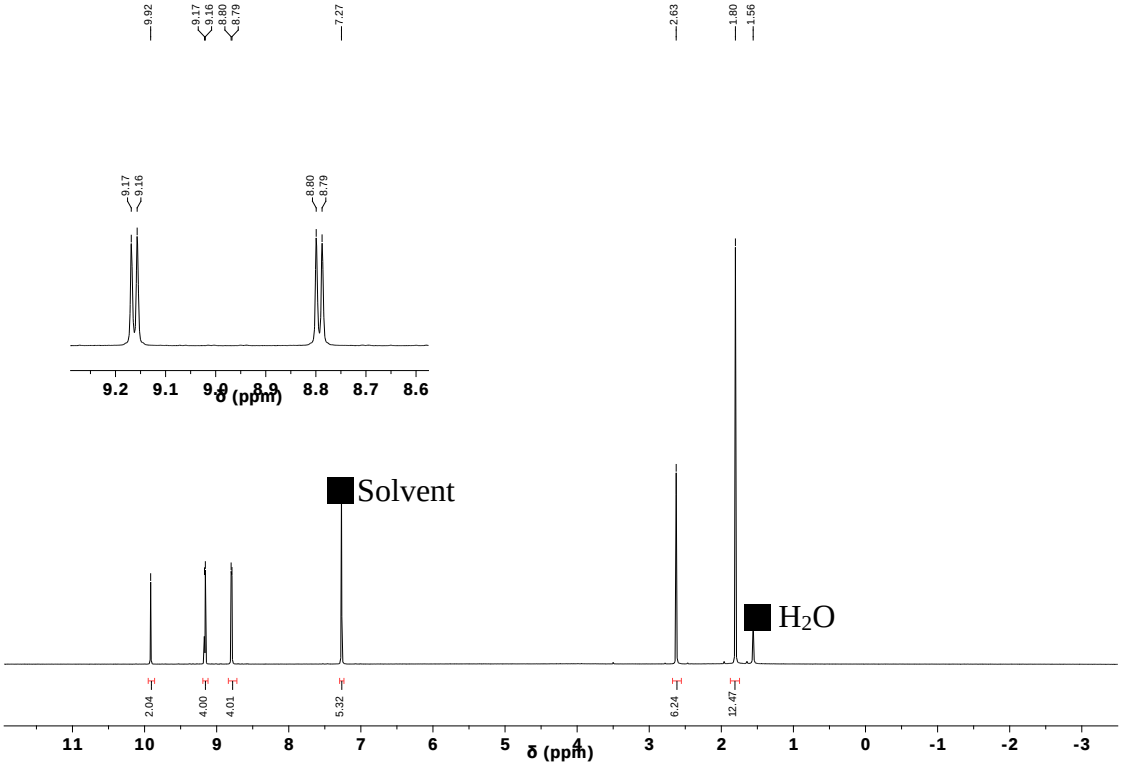

Figure S1. ^{1}H-NMR spectrum of compound **2** (400 MHz, $CDCl_3$).

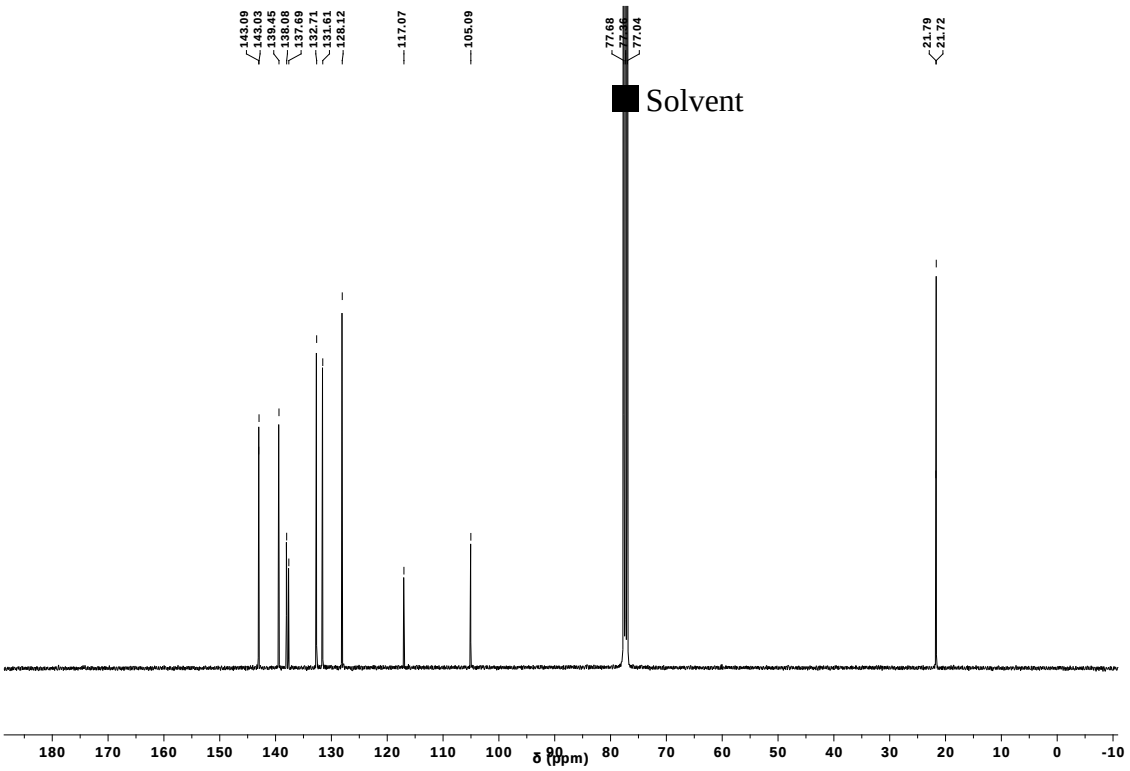

Figure S2. ^{13}C-NMR spectrum of compound **2** (100 MHz, $CDCl_3$).

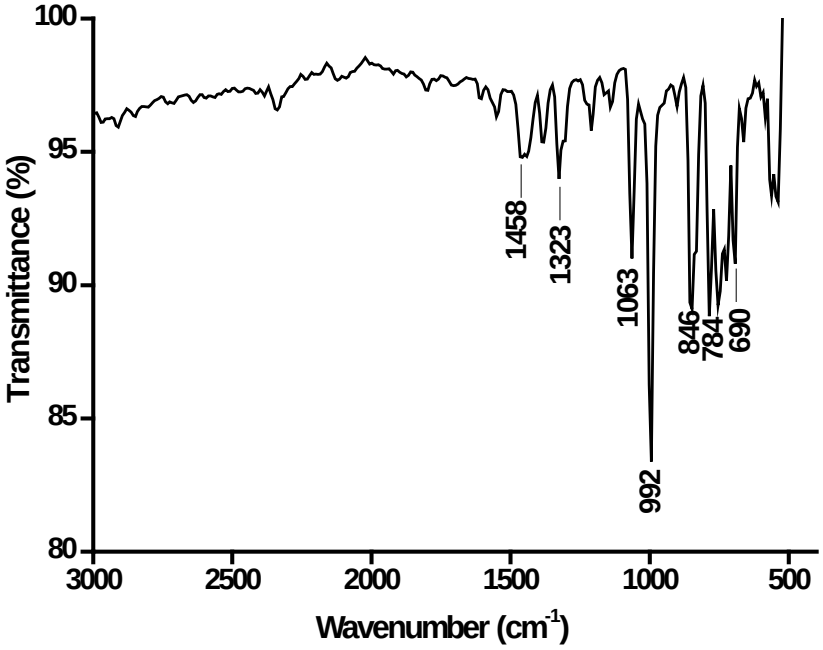

Figure S3. FT-IR spectrum of compound **2** (ATR).

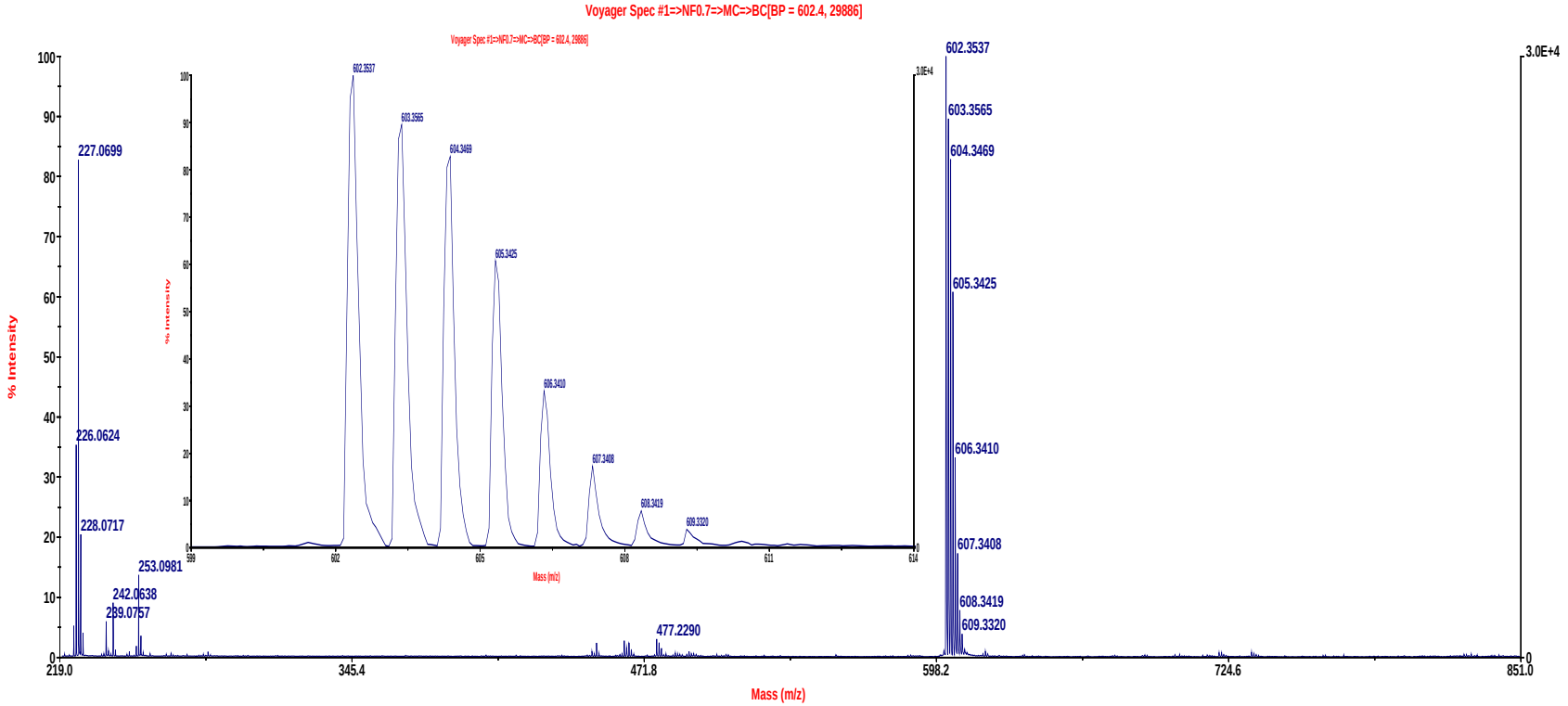

Figure S4. MALDI-TOF MS spectrum of compound **2**.

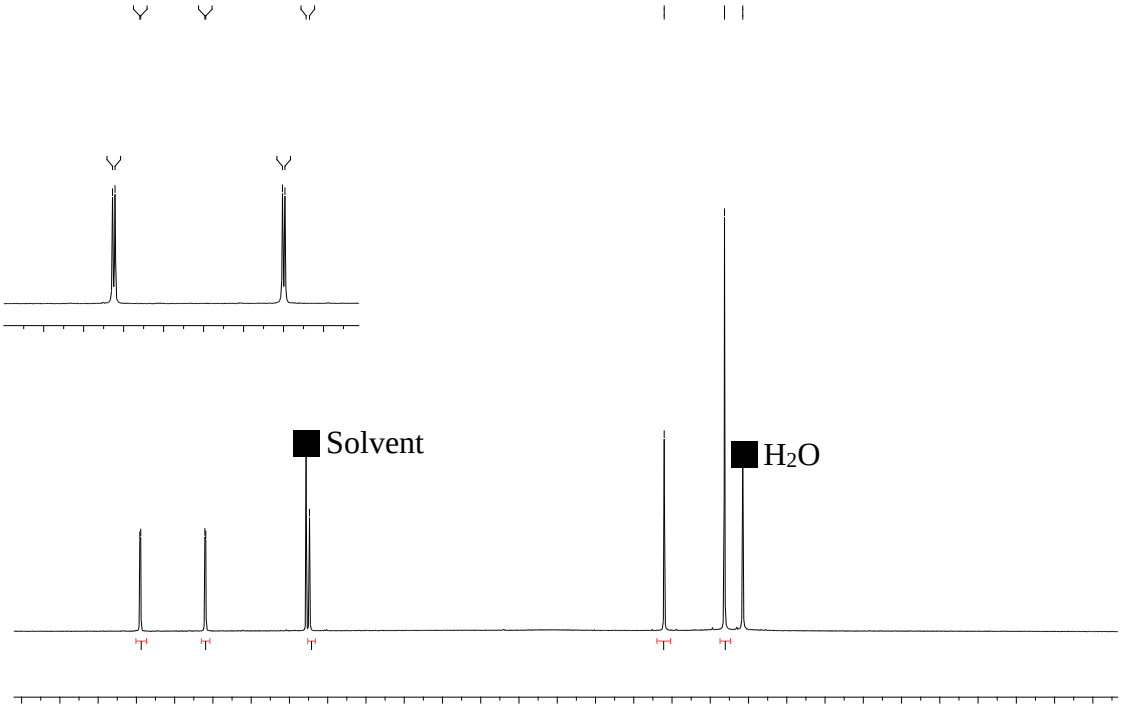

Figure S5. ^{1}H-NMR spectrum of compound **3** (400 MHz, $CDCl_3$).

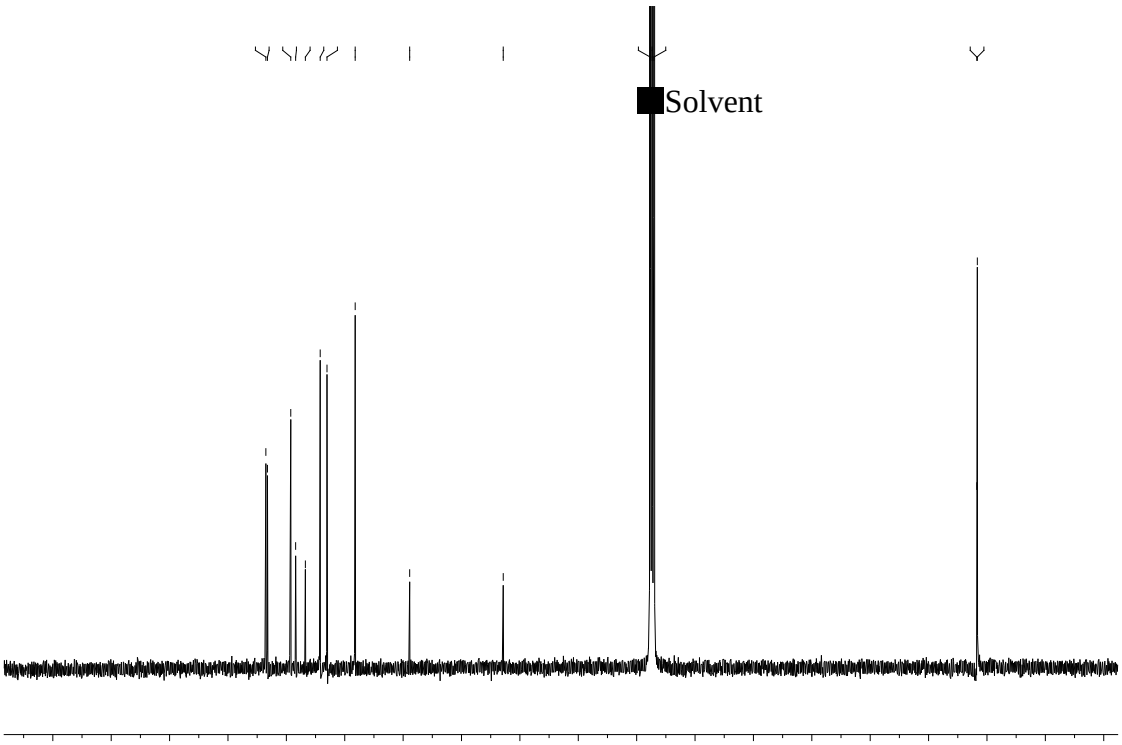

Figure S6. ^{13}C-NMR spectrum of compound **3** (100 MHz, $CDCl_3$).

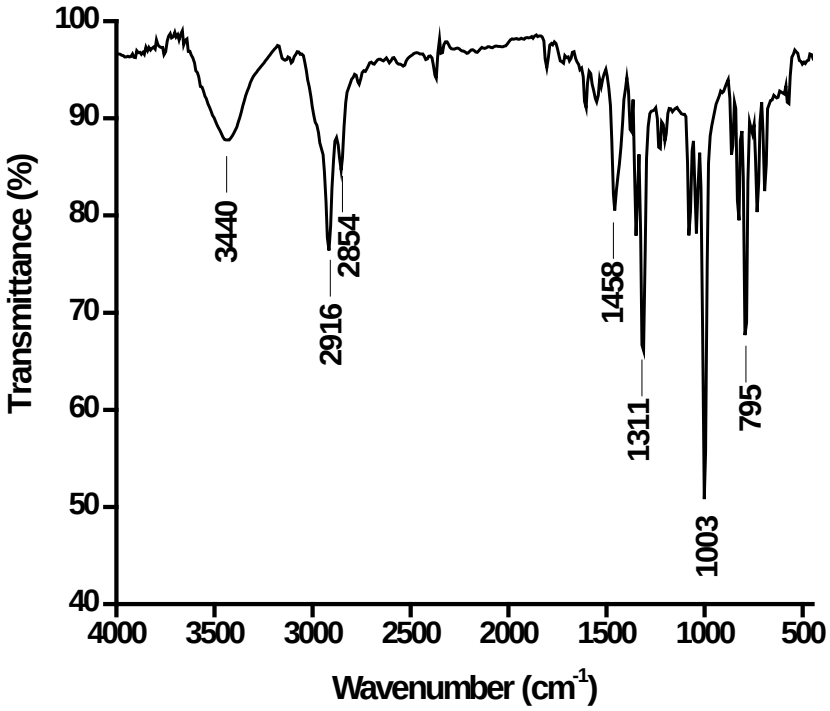

Figure S7. FT-IR spectrum of compound **3** (KBr).

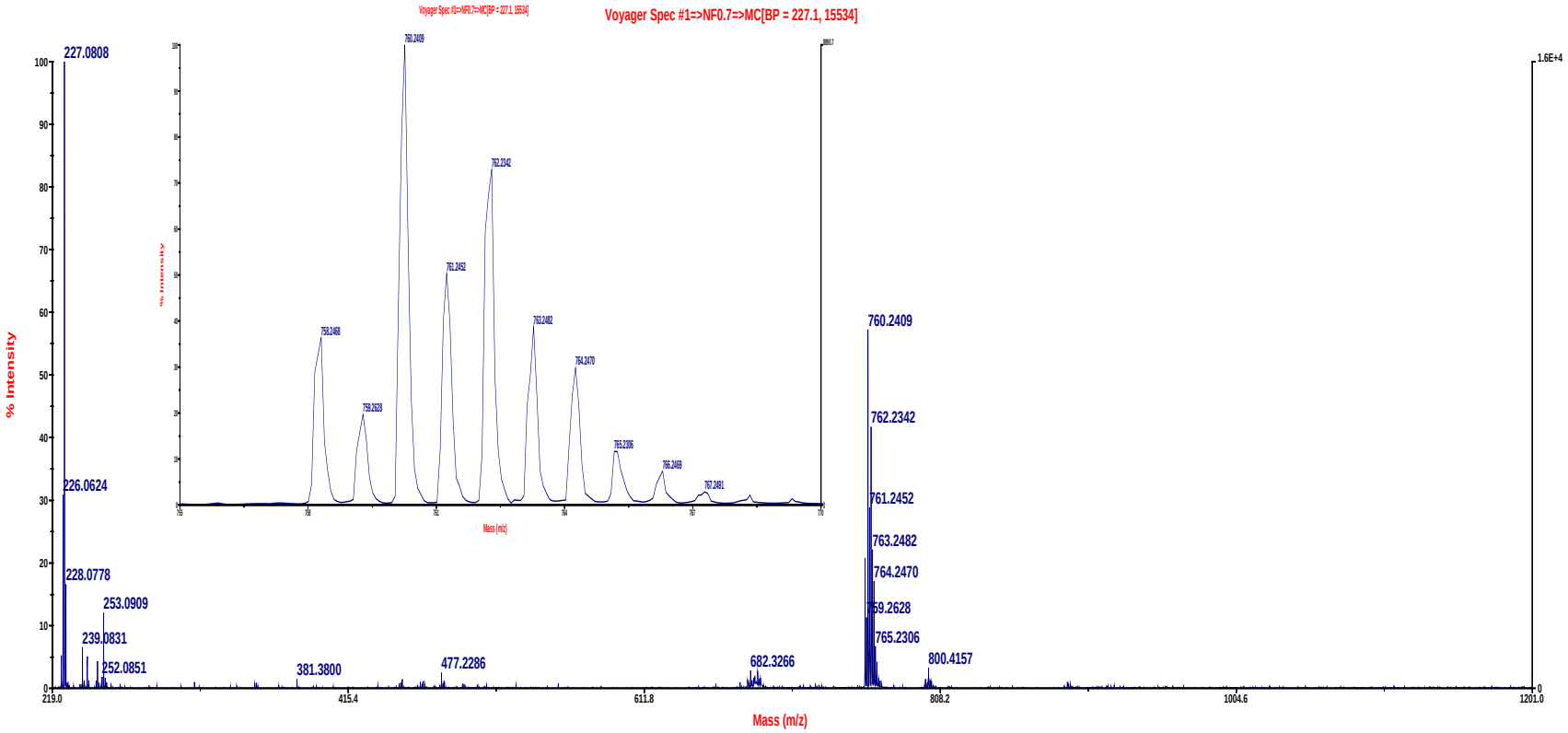

Figure S8. MALDI-TOF MS spectrum of compound **3**.

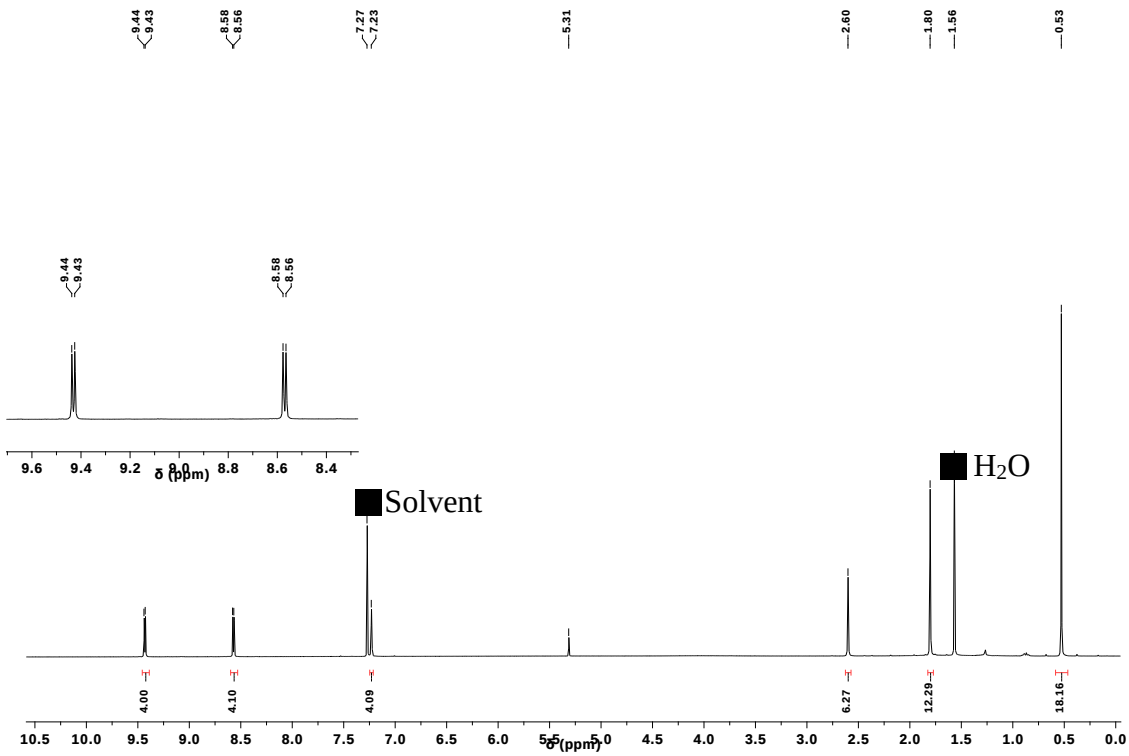

Figure S9. ^{1}H-NMR spectrum of compound **4** (400 MHz, $CDCl_3$).

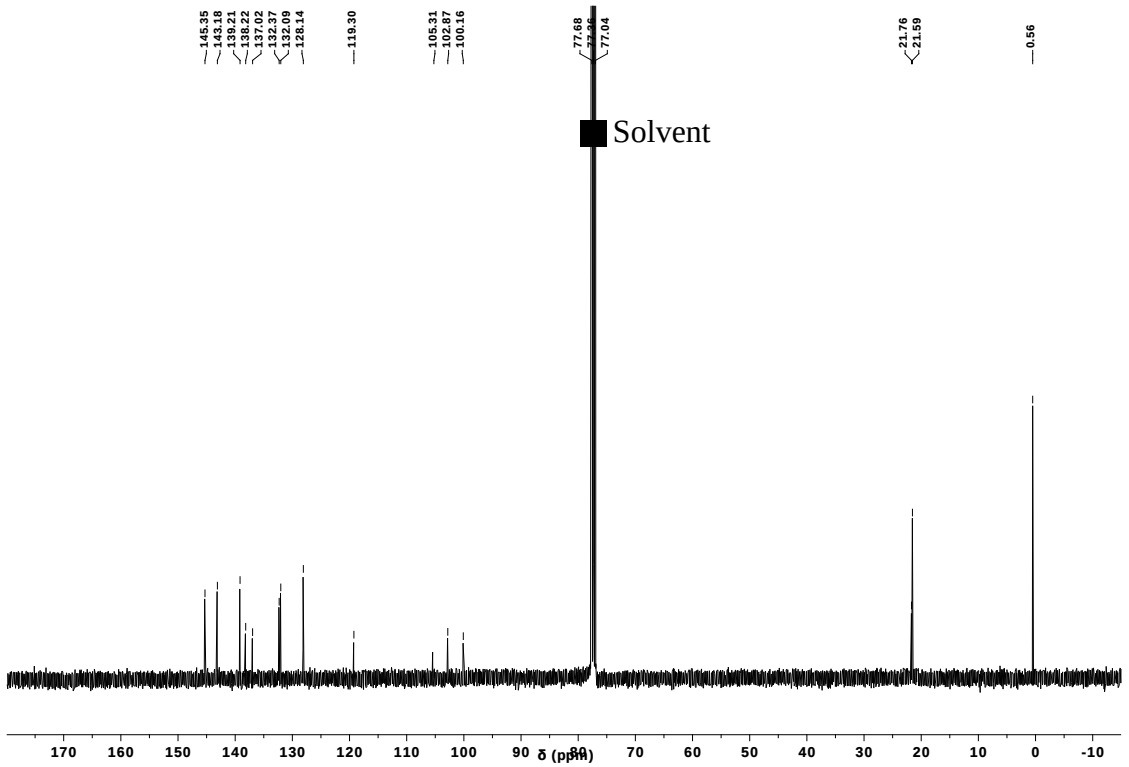

Figure S10. ^{13}C-NMR spectrum of compound **4** (100 MHz, $CDCl_3$).

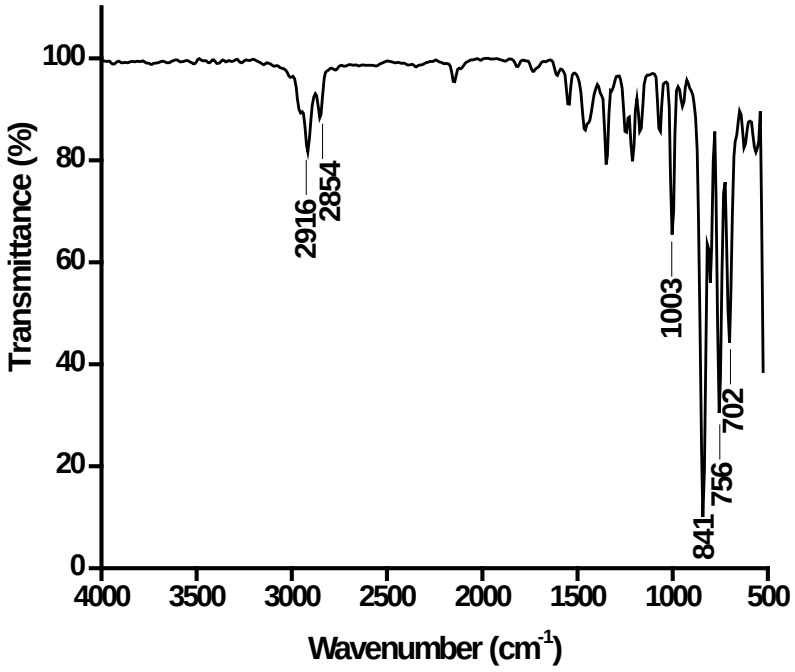

Figure S11. FT-IR spectrum of compound **4** (ATR).

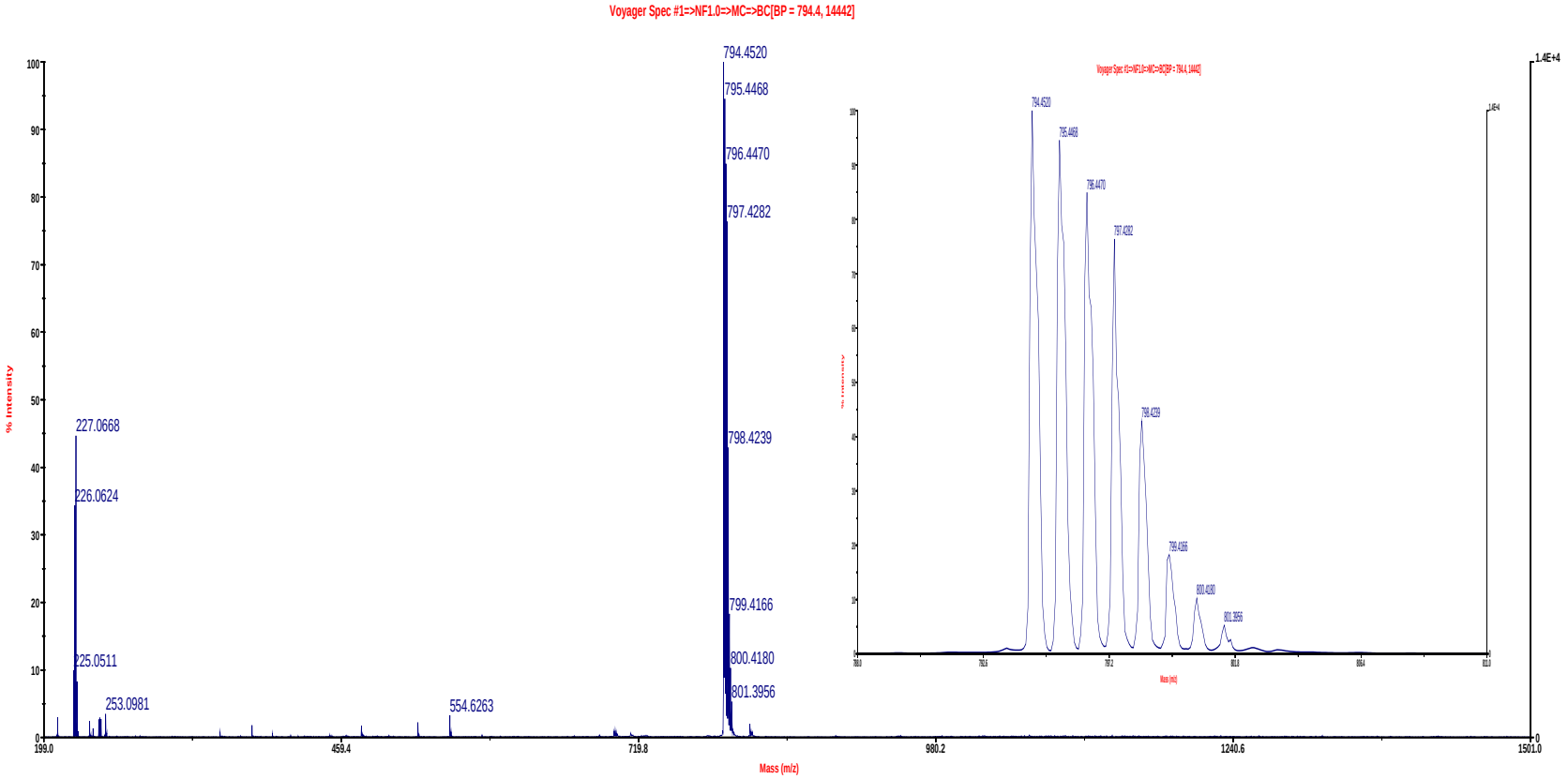

Figure S12. MALDI-TOF MS spectrum of compound **4**.

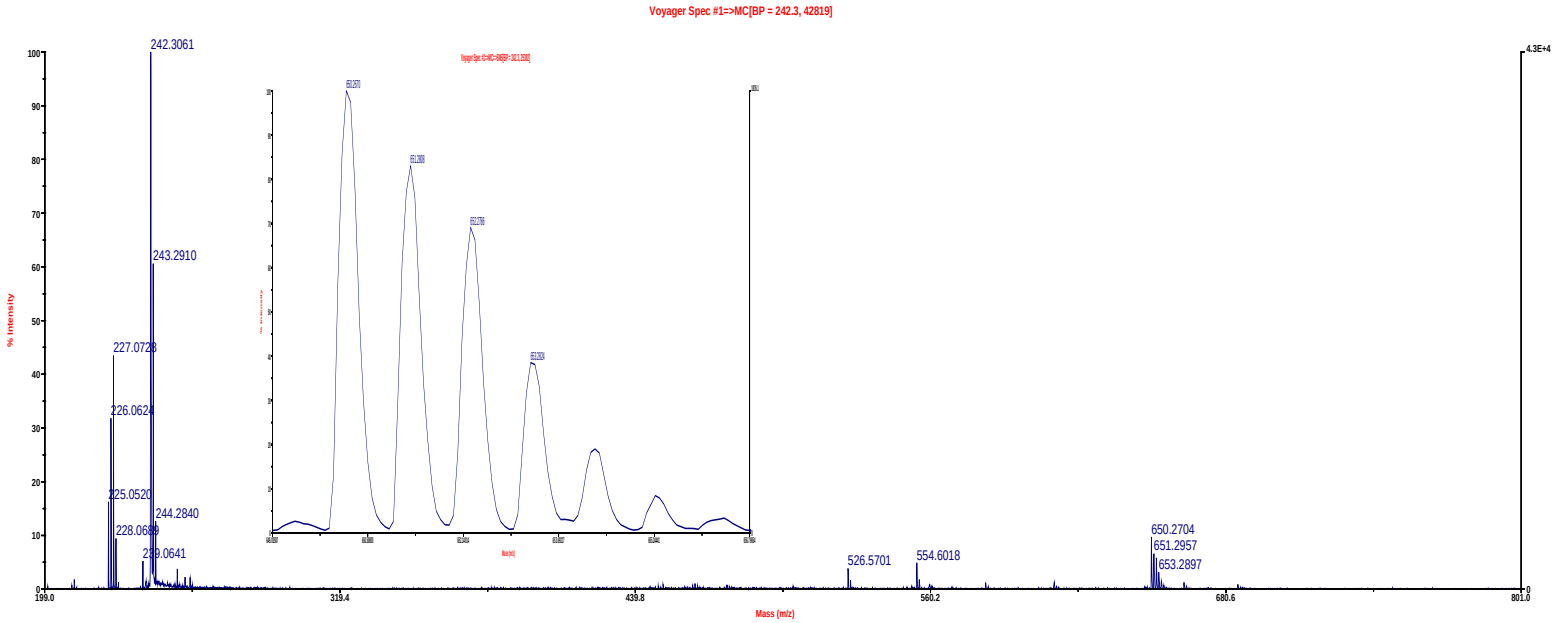

Figure S13. MALDI-TOF MS spectrum of compound **5**.

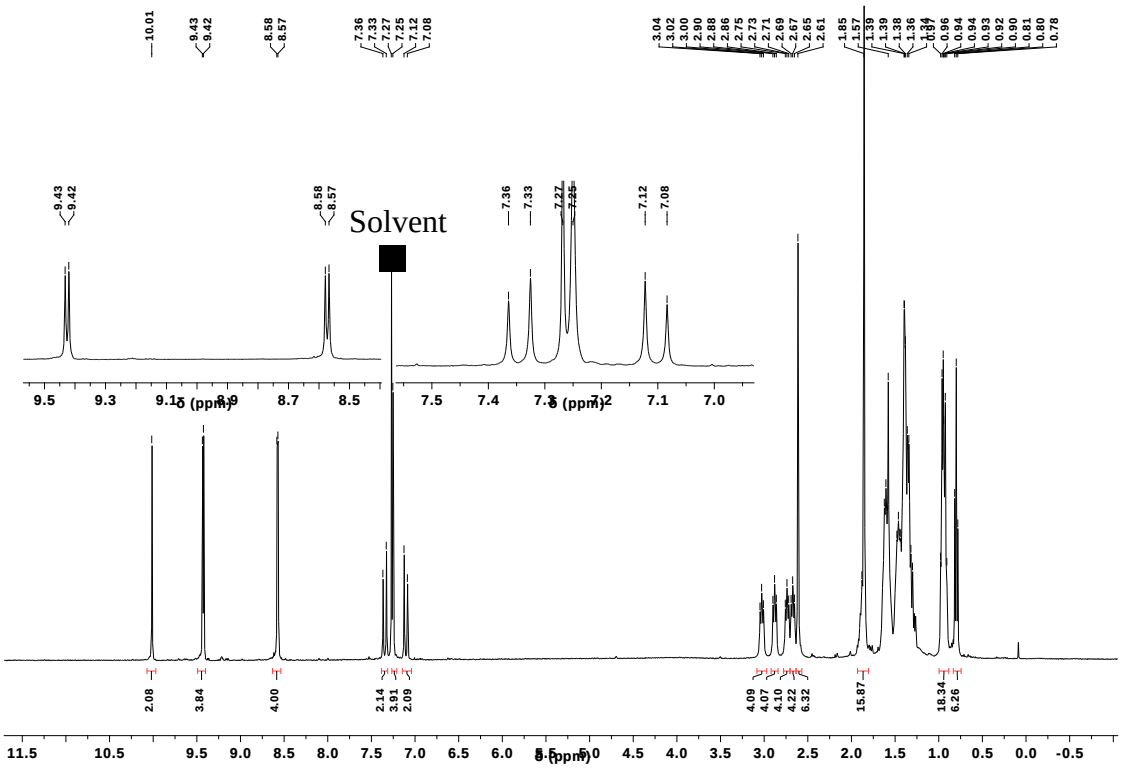

Figure S14. ^{1}H-NMR spectrum of compound **7** (400 MHz, $CDCl_3$).

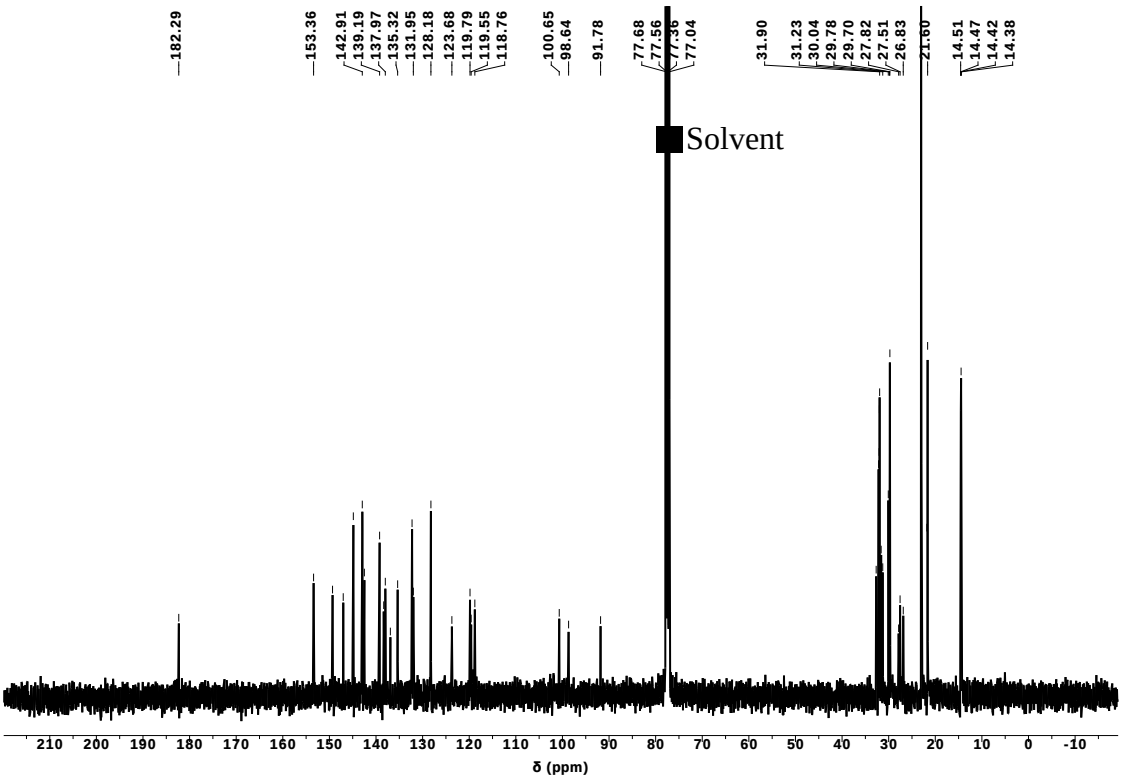

Figure S15. ^{13}C-NMR spectrum of compound **7** (100 MHz, $CDCl_3$).

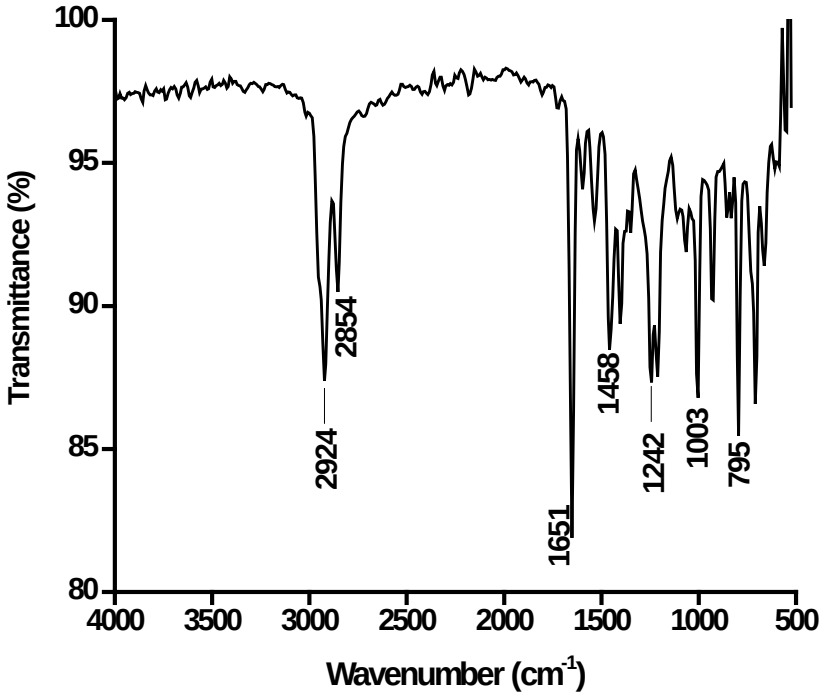

Figure S16. FT-IR spectrum of compound **7** (ATR).

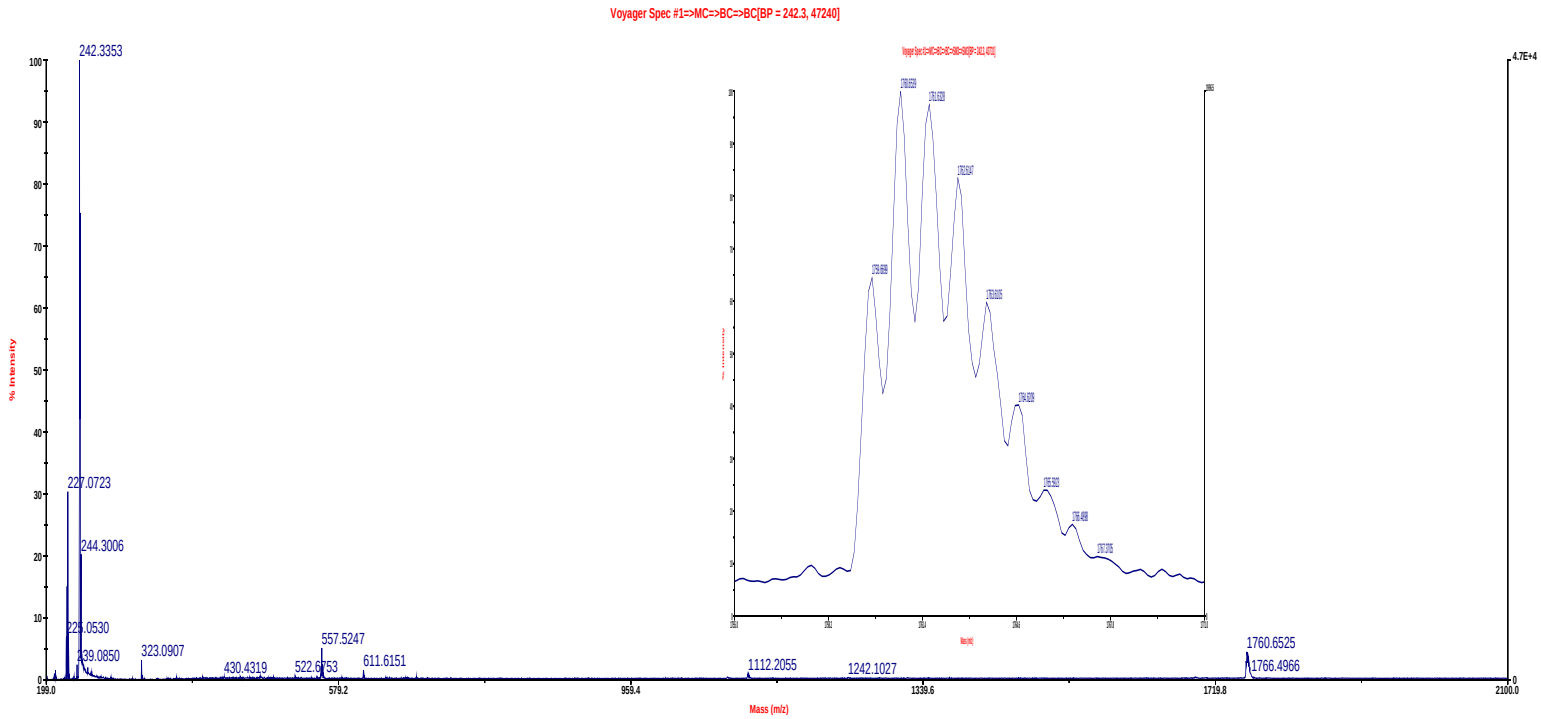

Figure S17. MALDI-TOF MS spectrum of compound **7**.

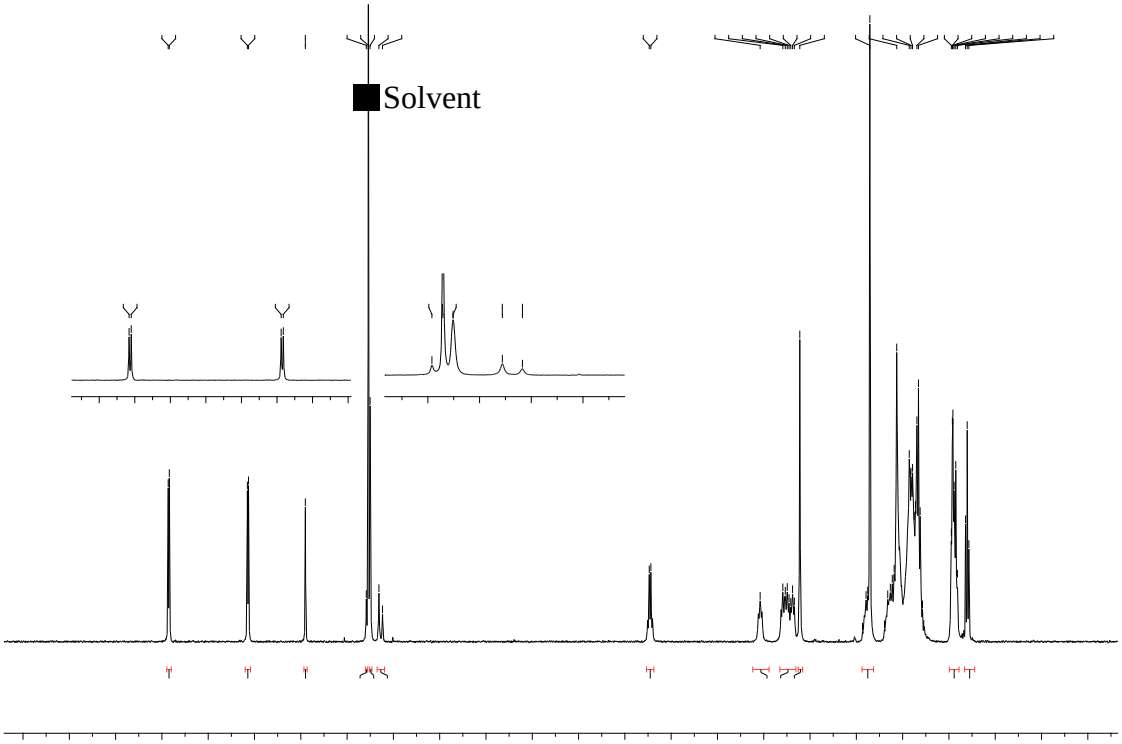

Figure S18. ^{1}H-NMR spectrum of **MV143** (400 MHz, $CDCl_3$)

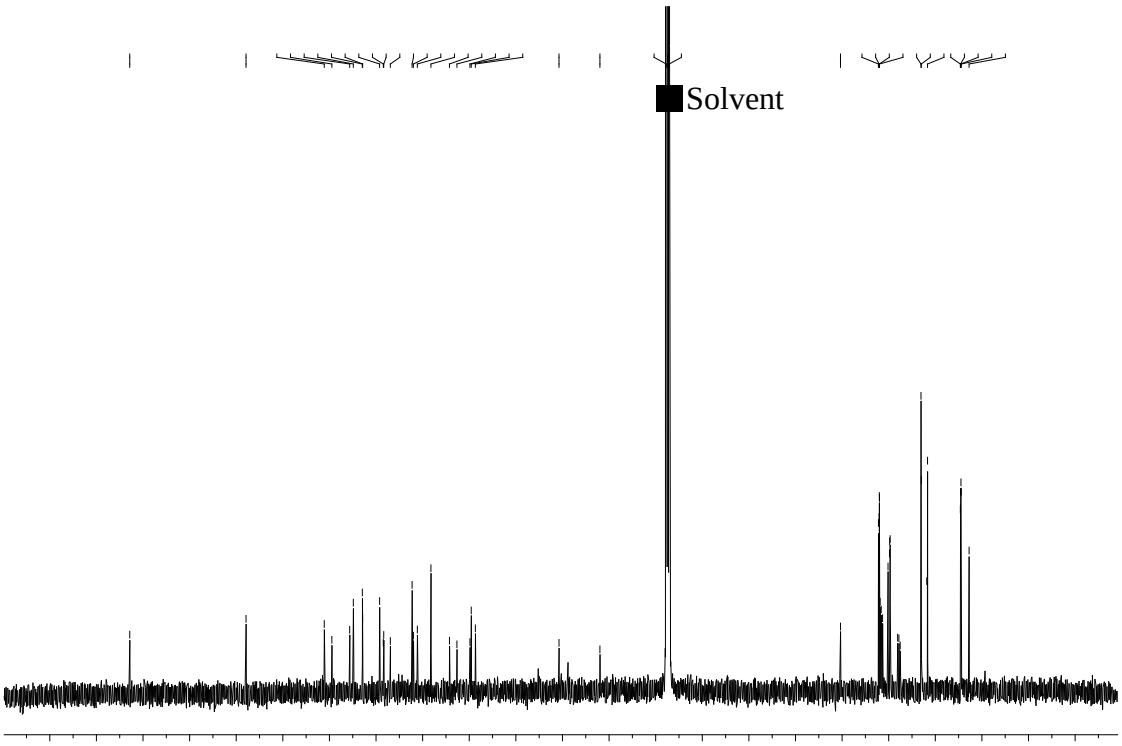

Figure S19. ^{13}C-NMR spectrum of **MV143** (100 MHz, $CDCl_3$).

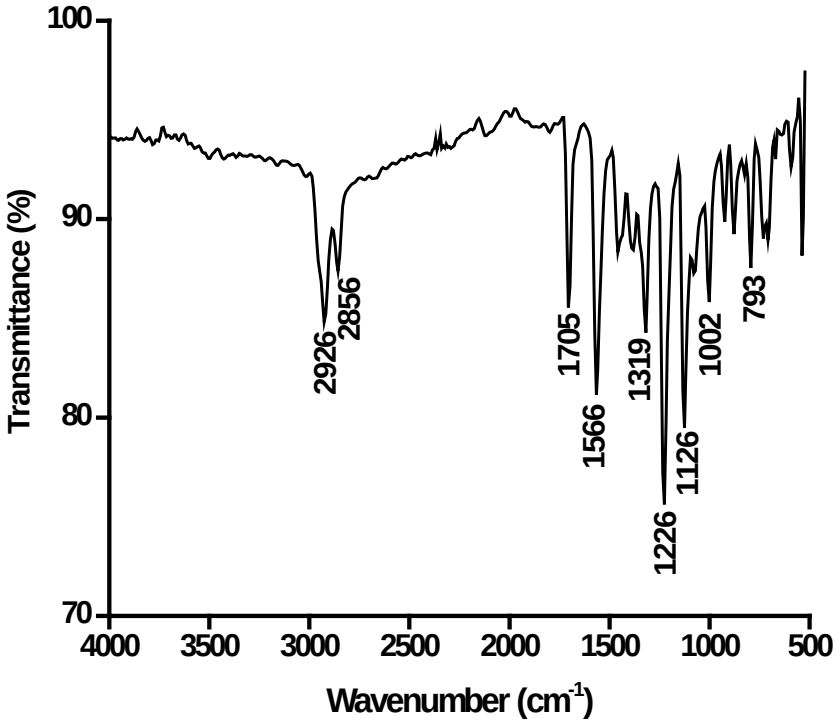

Figure S20. FT-IR spectrum of **MV143** (ATR).

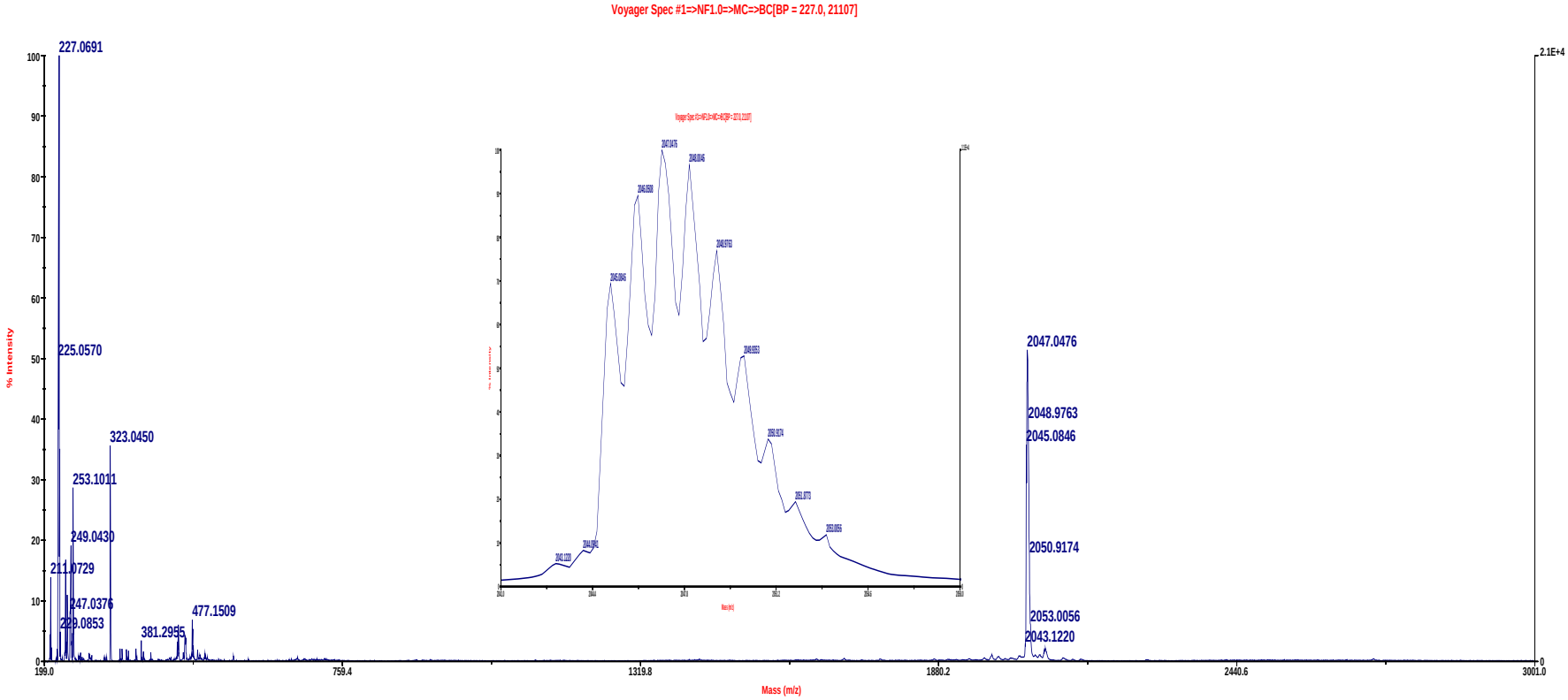

Figure S21. MALDI-TOF MS spectrum of compound **MV143**.

4. Thermogravimetric Analysis of compound MV143

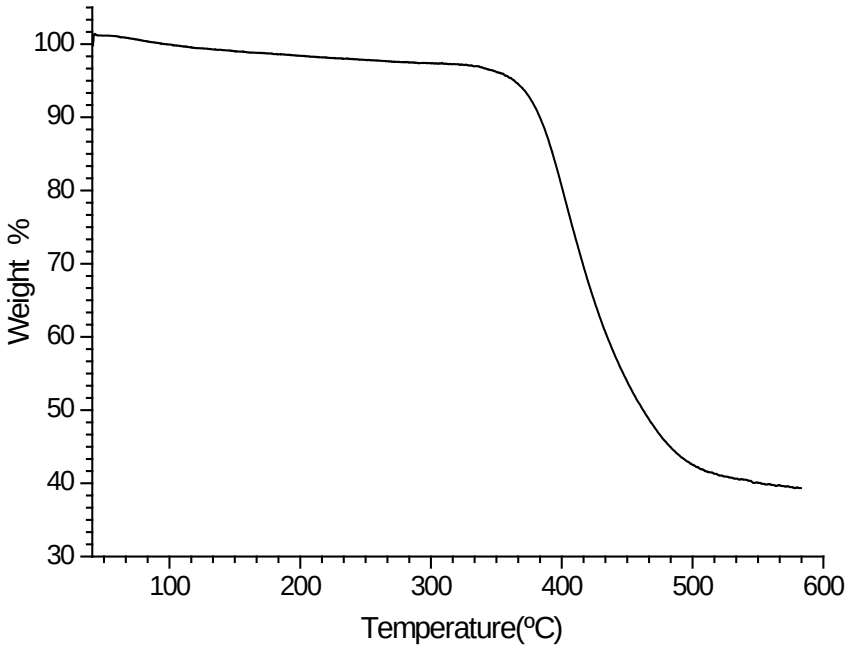

Figure S22. Thermogravimetric analysis plot of **MV143** (at 95 % Weight, T = 364°C).

5. Absorption spectra in solvents and in film.

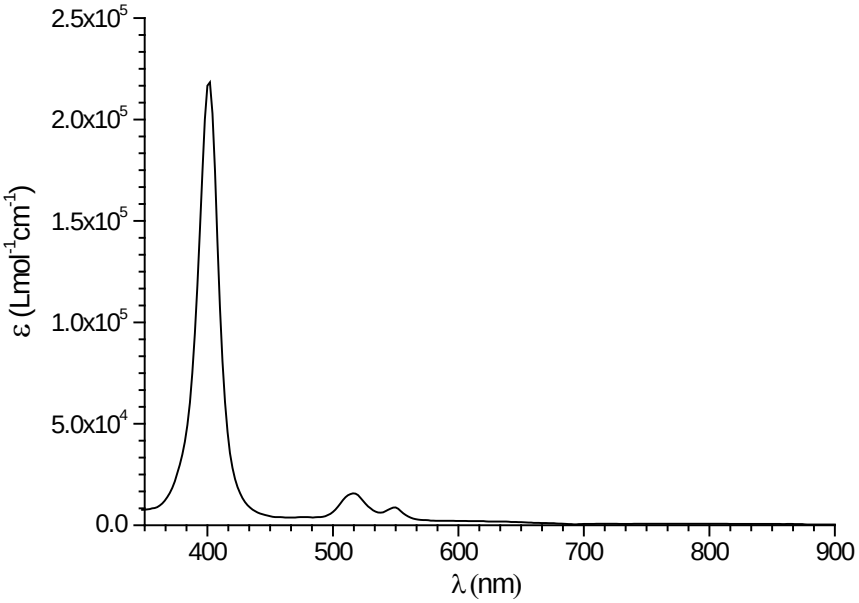

Figure S23. Absorption spectrum of compound **2** (10^{-6} M) in CH_2Cl_2.

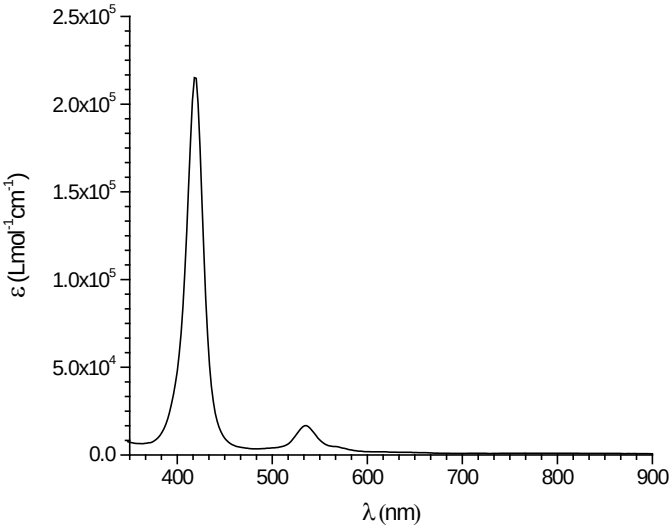

Figure S24. Absorption spectrum of compound **3** (10^{-6} M) in CH_2Cl_2.

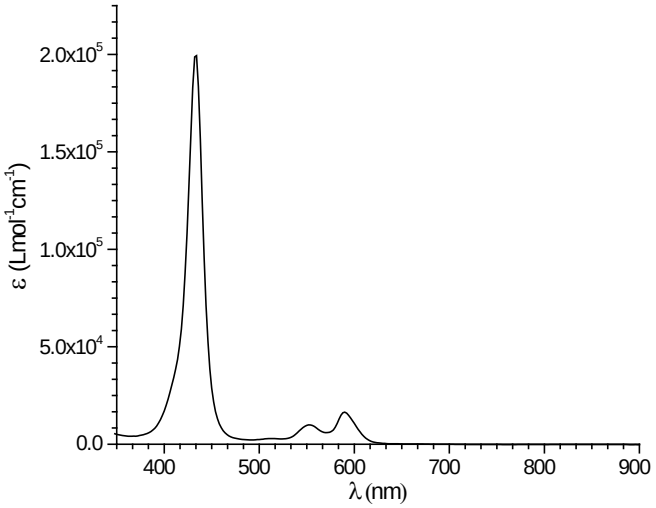

Figure S25. Absorption spectrum of compound **4** (10^{-6} M) in CH_2Cl_2.

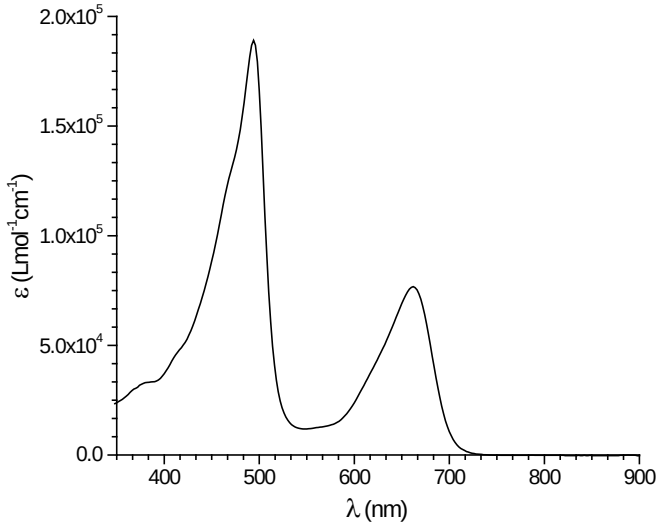

Figure S26. Absorption spectrum of compound **7** (10^{-6} M) in CH_2Cl_2.

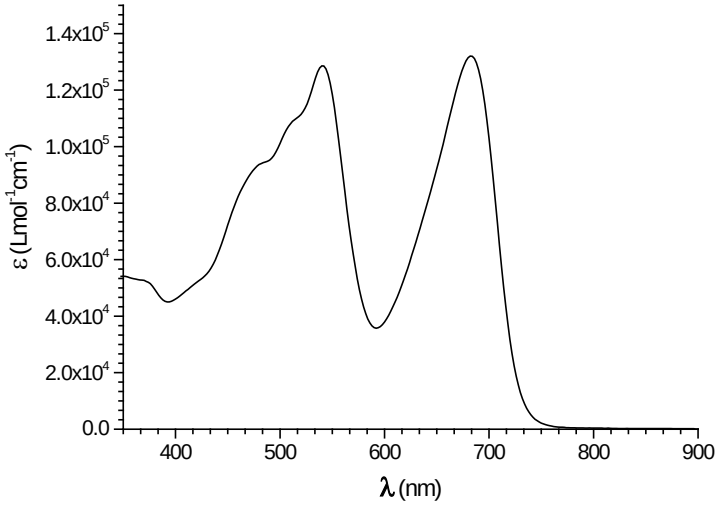

Figure S27. Absorption spectrum of **MV143** (10^{-6} M) in CH_2Cl_2.

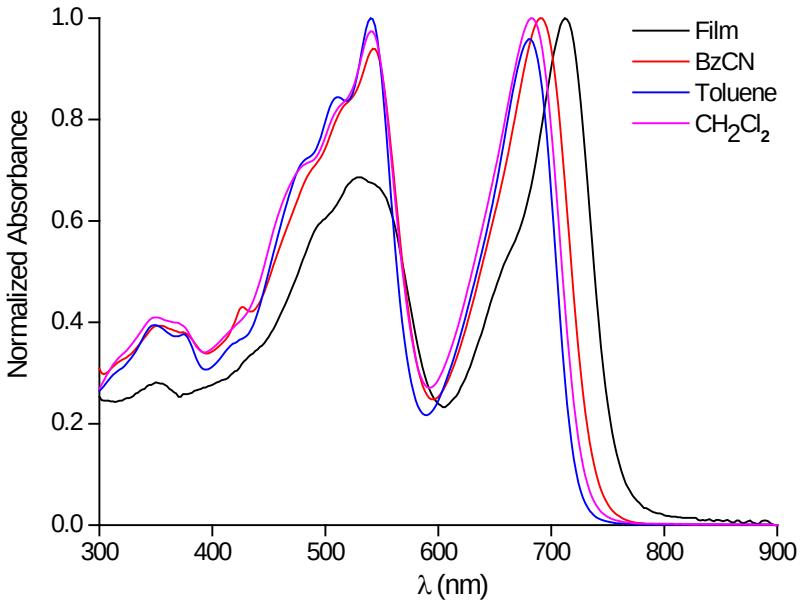

Figure S28. Absorption spectra of **MV143** in different solvents (10^{-6} M), toluene (blue), benzonitrile (BzCN) (red), CH_2Cl_2 (magenta), and in film (black).

6. Electrochemical Studies

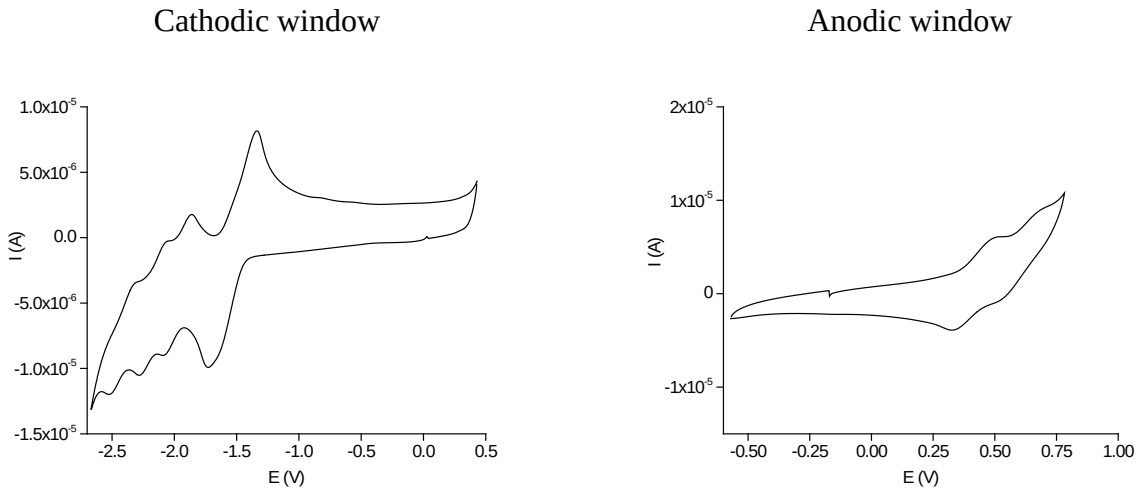

Figure S29. Cyclic Voltammetry (CV) plots of **MV143**.

Table S1. Optical properties and half-wave redox properties of **MV143** and MV71.

Molecule	λ_{abs} / nm (log ε)[a]	λ_{abs} / nm (film)	E^1_{ox}[b] (V)	E^1_{red}[b] (V)	E_{HOMO}[d] (eV)	E_{LUMO}[e] (eV)	E_g[f] (eV)
MV143	540 (5.11) 682 (5.12)	528 714	0.43[c]	–1.61[c]	–5.53	–3.49	2.04
MV71	547 (5.0) 716 (5.0)	540 762	0.14[c]	-1.60	-5.24	-3.55	1.69

[a] 10^{-6} M in dichloromethane; [b] 10^{-3} M in ODCB–acetonitrile (4:1) versus Fc^+/Fc (E_{ox} = 0.07 V) glassy carbon, Pt counter electrode, 20 °C, 0.1 M Bu_4NClO_4, and scan rate = 100 mV s^{-1}; [c] Reversible processes; [d] Estimated from $E_{HOMO} = -5.1 - E^1_{ox}$; [e]Estimated from $E_{LUMO} = -5.1 - E^1_{red}$; [f] $E_g = E_{LUMO} - E_{HOMO}$.

7. Theoretical calculations

Theoretical calculations were carried out (Gaussian 09, DFT B3LYP/6-31G level of theory) in order to study the influence of the Ni atom on the optimized geometry of the porphyrin macrocycle in **MV143**. As shown in Figure S30, and in contrast to the analogous Zn-porphyrin-based A-π-D- π-A small molecule **MV71**, which is planar,[1] the Ni-porphyrin-based **MV143** has a ruffled structure.

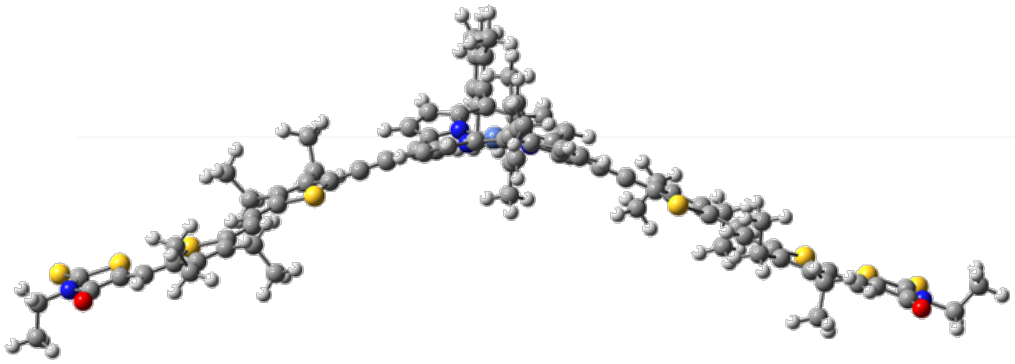

Figure S30. Optimized geometry of **MV143**.

The metal ion can induce a distortion of the porphyrin plane due to the number of d-electrons or, more specifically, the occupancy of the metal d-orbitals.[2,3] Zn(II) porphyrins have fully occupied d-orbitals (d^{10}) and, as a consequence, the M–N bond length increases and is close to the optimal bond length to retain the planarity of the macrocycle (2.01 Å).[4] In the case of the Ni(II) porphyrin, the core size is smaller due to the d^8 singlet configuration of Ni(II), which leaves the $d_{x^2-y^2}$ orbital unoccupied.

The data obtained from the theoretical calculations for **MV71** and **MV143** are consistent with the above hypothesis. The optimal bond length is similar to that calculated for four-coordinated Zn(II) porphyrin **MV71** (Figure S31), which has a planar structure with an average Zn–N bond length of

2.05 Å and dihedral angles for all pyrrole rings close to 0º. As a result the porphyrin ring is almost planar.

However, the Ni(II) porphyrin macrocycle in **MV143** has Ni–N bond distances of 1.92 Å, i.e., smaller than those calculated for **MV71**, and an out of plane distortion of the pyrrole rings is observed (Figure S32). In addition, there is a difference between the angles of the pyrrole ring that bears phenyl substituents in *meso* positions of the porphyrin (6.7–7.0 Å) and those that are bonded to the ethynyl group (~10 Å).

The π-conjugated system bonded to the porphyrin core is almost planar in both compounds (**MV71** and **MV143**) and this allows the electronic delocalization between the porphyrin core and the end-capped acceptor fragments.

The theoretical electronic density contours of the HOMO and LUMO calculated for **MV71** and **MV143** are shown in Figure S33. Both orbitals are spread along the π-conjugated system with an overlap between them, thus favoring HOMO-LUMO electronic transitions.

Bond lengths Zn-N: 2.05 Å

Dihedral angles (º)

$N_{41}C_{24}\mathbf{C_{22}}C_{23}$: 0.30

$N_{41}C_{42}\mathbf{C_{45}}C_{38}$: -0.21

$N_{28}C_{23}\mathbf{C_{22}}C_{24}$: 0.03

$N_{28}C_{27}\mathbf{C_{29}}C_{30}$: -0.09

$N_{31}C_{30}\mathbf{C_{29}}C_{27}$: -0.09

$N_{31}C_{33}\mathbf{C_{35}}C_{36}$: -0.03

$N_{37}C_{36}\mathbf{C_{35}}C_{33}$: -0.33

$N_{37}C_{38}\mathbf{C_{45}}C_{48}$: -0.21

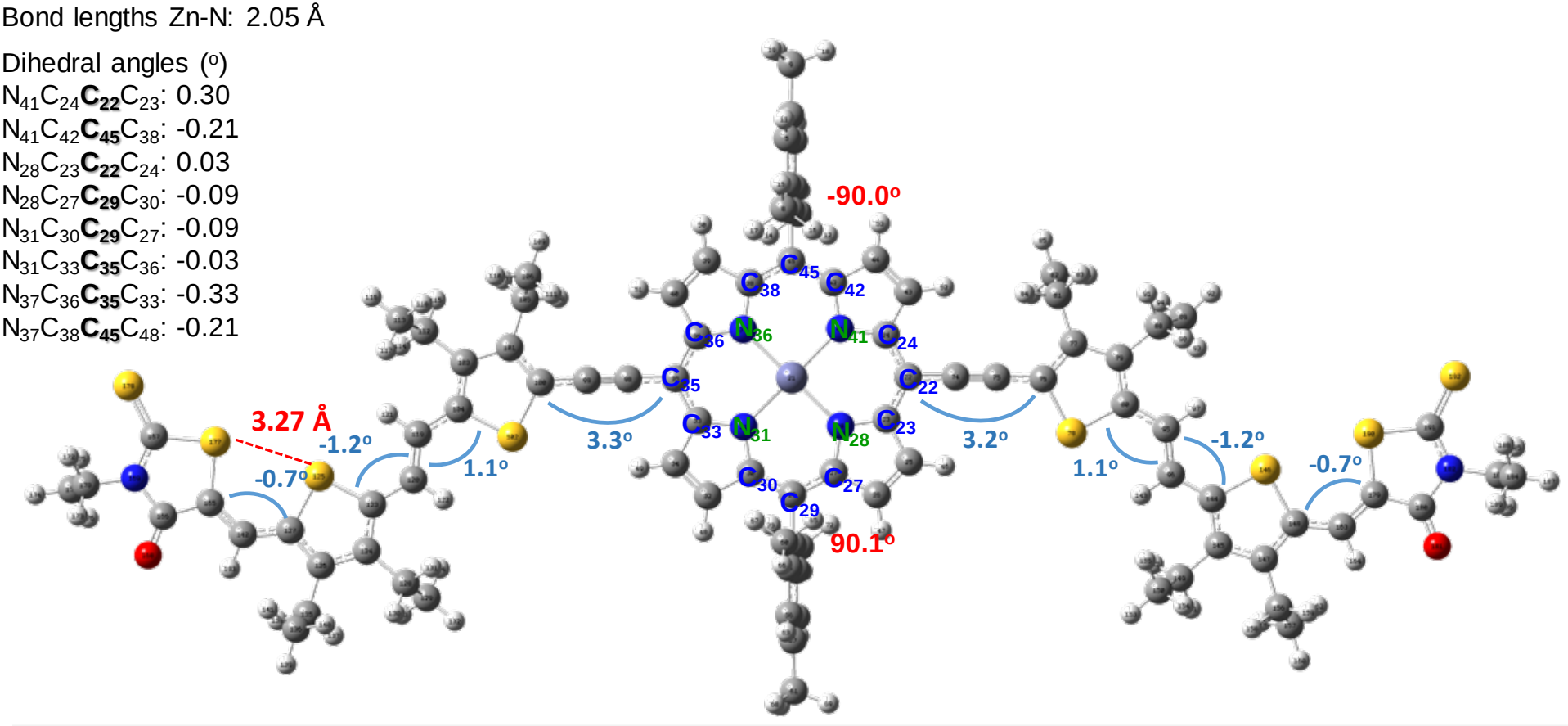

Figure S31. Optimized geometry of compound **MV71**.

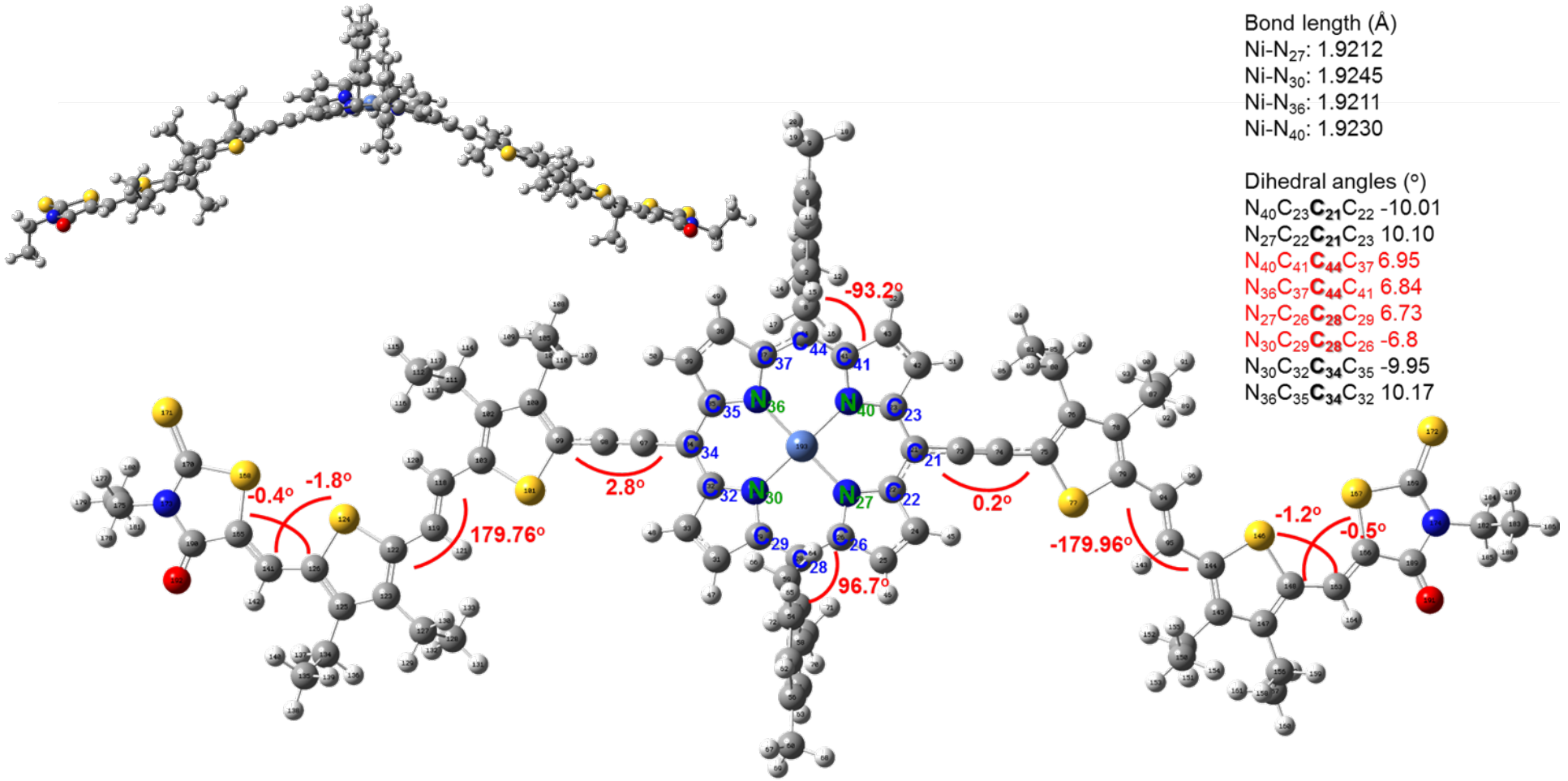

Figure S32. Optimized geometry of compound **MV143**.

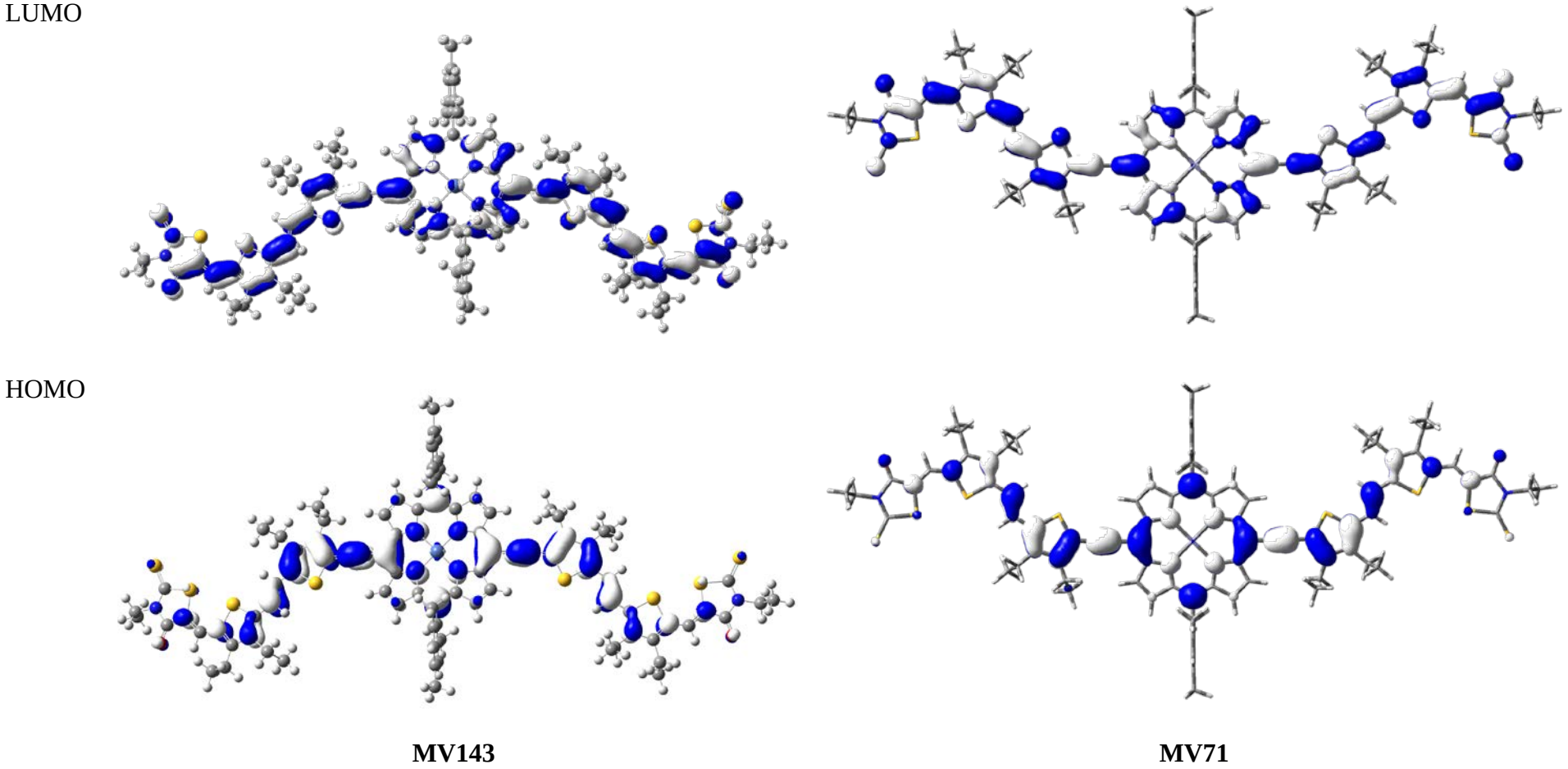

Figure S33. HOMO and LUMO electron density of **MV143** and **MV71**.

8. Photovoltaic Studies.

a. Absorption spectrum of active layer.

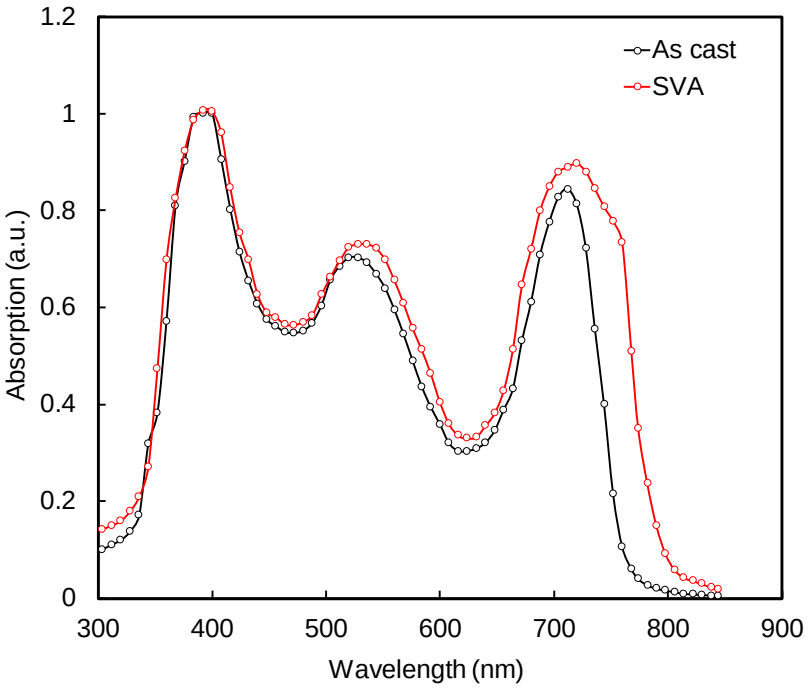

Figure S34. Optical absorption spectra of as-cast and SVA-treated **MV143**:$PC_{71}BM$ thin films.

b. Hole and electron mobilites

The plots were fitted with the space charge limited current model; the hole/electron mobility values are $1.45 \times 10^{-5}/2.28 \times 10^{-4}$ cm^2/Vs and $1.08 \times 10^{-4}/2.41 \times 10^{-4}$ cm^2/Vs for as-cast and SVA-treated **MV143**:PC71BM active layers, respectively. Both, the hole and electron mobility, in the blend film were enhanced after SVA treatment, but the increase in hole mobility was more marked than that of the electron mobility. Moreover, the ratio of electron to hole mobility decreased to 2.23 for the SVA-treated device as compared to 15.2 for as-cast counterpart (Figure S35).

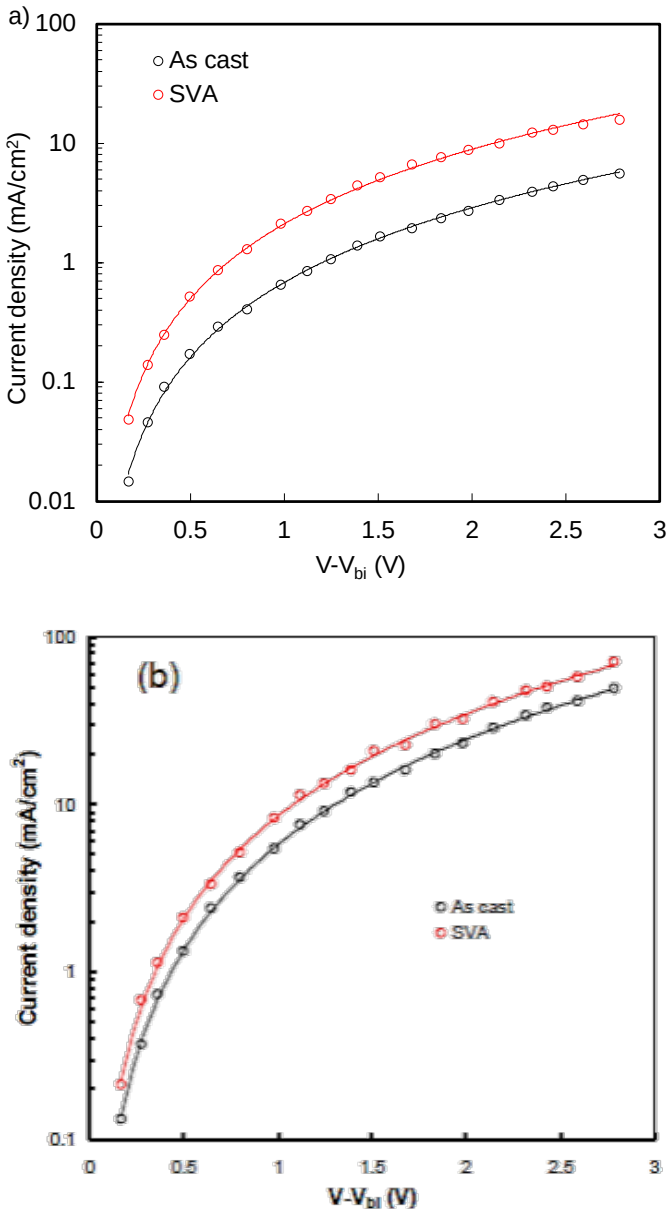

Figure S35. Dark J-V characteristics of (a) hole only and (b) electron only devices processed with as-cast and SVA-treated **MV143**:$PC_{71}BM$ active layers, solid lines represent the SCLC fitting.

c. Measurement of J_{SC} and V_{OC} at different illumination intensities.

The J_{SC} and V_{OC} were also measured at different illumination intensities (P_{in}) for the OSCs to investigate the effect of SVA on the charge recombination mechanism. The results are shown in Figure S36. The relationship between the J_{SC} and P_{in} (Figure S36a) can be expressed as $J_{sc} \propto (P_{in})^{\gamma}$,[5,6] where γ is the factor whose value indicates the degree of recombination. When γ is equal to unity it indicates that all of the charges in the active layer were extracted by the electrodes without any bimolecular recombination. In contrast, if γ is less than unity there is bimolecular charge

recombination before charges are collected at the electrodes. The value for the device based on the SVA-treated active layer is around 0.957, which indicates that the molecular recombination is effectively suppressed, whereas the value of γ for the as-cast counterpart is around 0.863, which indicates a higher degree of bimolecular recombination.

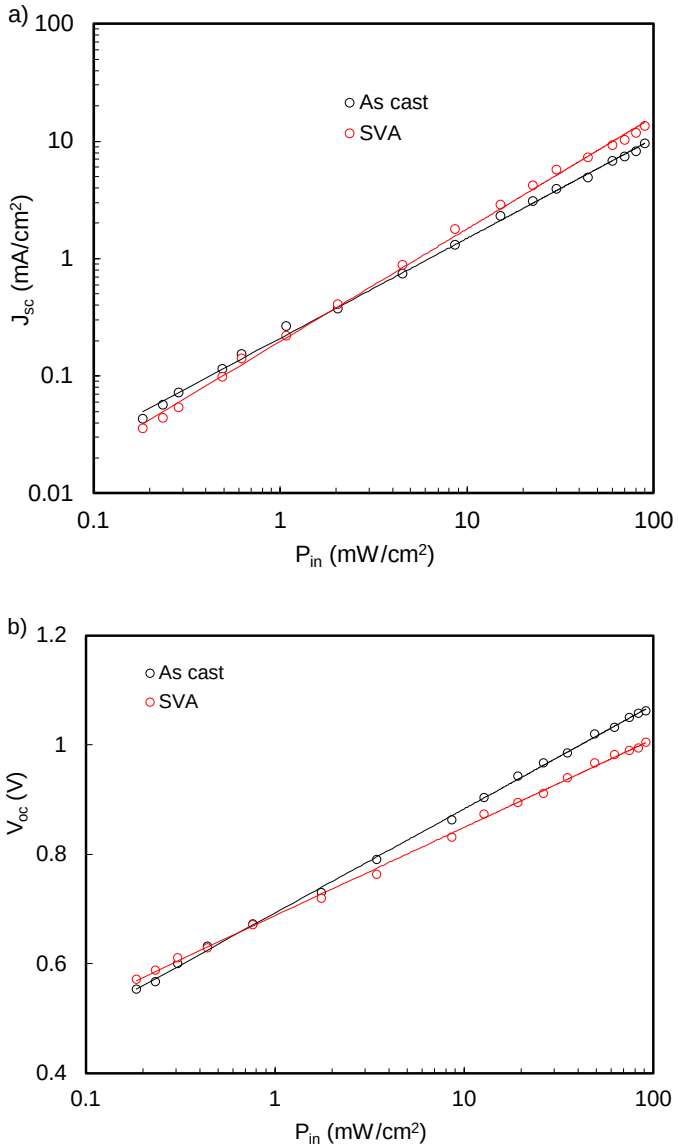

Figure S36. Variation of (a) J_{SC} and (b) V_{OC} with illumination intensity (P_{in}) for the OSCs processed with as-cast and SVA-treated **MV143**:$PC_{71}BM$ active layers.

The variation of V_{OC} with P_{in} in a semi-logarithmic plot is shown in Figure S36b and this also provides information about the degree of trap-assisted recombination. The relationship between V_{OC} and P_{in} is described as:

$$V_{oc} \propto nkT/q \ln(P_{in})$$

where k is Boltzmann's constant, T is the temperature, n is the diode ideality factor and q is the electronic charge. When the value of n is around unity the bimolecular recombination is dominant in

the OSCs. However, if the value of n is around two, then trap-assisted or Shockley–Read–Hall (SRH) recombination is the dominant process. The calculated *n* values for as-cast and SVA-treated OSCs are around 1.49 and 1.21, respectively. The high *n* value for the as-cast device indicates that there is considerable trap-assisted recombination in this device, under open circuit voltage, and this may be related to poor morphology and lower charge carrier mobility, which results in significant charge accumulation and therefore poor charge extraction. However, the n value is 1.21 for the SVA counterpart and this indicates that bimolecular recombination is dominant and trap-assisted recombination is reduced due to the improved morphology of the active layer and more balanced charge transport.

It is observed that the V_{OC} for the optimized **MV143** based OSC (1.08 V) is higher than that for **MV71** counterpart (0.85 V) and attributed to the deeper HOMO energy level of **MV143** as discussed earlier. However, the J_{SC} value of **MV143** based OSC is slightly lower than that for **MV71** based device although the LUMO offset value for **MV143**:$PC_{71}BM$ (0.61 eV) is larger than that for **MV71**:$PC_{71}BM$ (0.55 eV), but the **MV71** exhibit the lower optical bandgap and broader optical absorption spectra in longer wavelength region than **MV143**, indicating that the light harvesting efficiency for the **MV71**:$PC_{71}BM$ based OSCs is larger than that for **MV143**:$PC_{71}BM$. However, the overall PCE for **MV143** based OSCs is higher than that for **MV71** counterparts, and mainly due to the higher value of V_{OC} for former devices. It is well known that there is a trade-off between J_{SC} and V_{OC} and thus minimizing this trade-off between to values is one of the most important issues in OSCs. A key issue to overcome this important issue in OSCs is to reduce the relatively large photon energy loss (E_{loss}) which is defined as E_g-qV_{OC}, where E_g is the optical band gap of the donor or acceptor employed in the active layer, whichever is small.[7–12] We have estimated the E_{loss} for the optimized OSCs employing **MV143** and **MV71** and are about 0.52 eV and 0.66 eV, respectively. The low E_{loss} is one of the reasons for the high value of V_{OC} for the OSC based on **MV143**, which is one of the key factors for the high value of PCE. Recently, Yang et. al have reported a low energy loss of 0.54 eV with high V_{OC} value of 1.15 V for all small OSCs employing non-fullerene acceptor,[13] whereas we have achieved even low value of energy loss of 0.52 eV for OSCs based on porphyrin small molecule as donor and $PC_{71}BM$ as acceptor.

d. TEM images of active layer

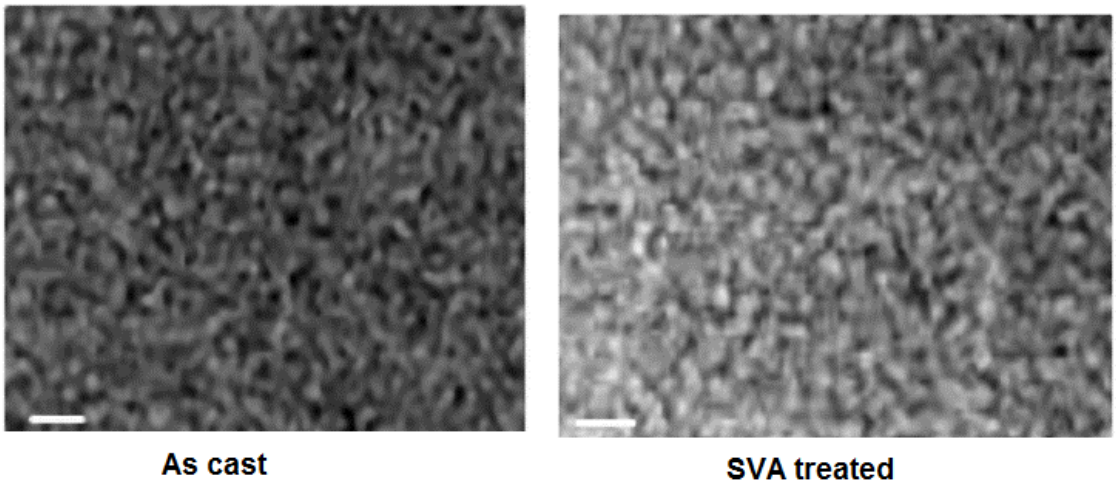

Figure S37. TEM images of the as cast and SVA treated **MV143**:$PC_{71}BM$ active layers (scale bar is 100 nm).

REFERENCES

1 N. F. Montcada, S. Arrechea, A. Molina-Ontoria, A. I. Aljarilla, P. de la Cruz, L. Echegoyen, E. Palomares and F. Langa, *Org. Electron.*, 2016, **38**, 330–336.

2 P. M. Kozlowski, J. R. Bingham and A. A. Jarzecki, *J. Phys. Chem. A*, 2008, **112**, 12781–12788.

3 Y.-H. Zhang, W. Zhao, J. Wang and P. Jiang, *Spectrochim. Acta Part A Mol. Biomol. Spectrosc.*, 2010, **75**, 499–506.

4 J. Schindler, S. Kupfer, A. A. Ryan, K. J. Flanagan, M. O. Senge and B. Dietzek, *Coord. Chem. Rev.*, 2018, **360**, 1–16.

5 H. Lin, S. Chen, Z. Li, J. Y. L. Lai, G. Yang, T. McAfee, K. Jiang, Y. Li, Y. Liu, H. Hu, J. Zhao, W. Ma, H. Ade and H. Yan, *Adv. Mater.*, 2015, **27**, 7299–7304.

6 Q. Wu, D. Zhao, A. M. Schneider, W. Chen and L. Yu, *J. Am. Chem. Soc.*, 2016, **138**, 7248–7251.

7 W. Li, K. H. Hendriks, A. Furlan, M. M. Wienk and R. A. J. Janssen, *J. Am. Chem. Soc.*, 2015, **137**, 2231–2234.

8 D. Veldman, S. C. J. Meskers and R. A. J. Janssen, *Adv. Funct. Mater.*, 2009, **19**, 1939–1948.

9 K. Kawashima, Y. Tamai, H. Ohkita, I. Osaka and K. Takimiya, *Nat. Commun.*, 2015, **6**, 10085.

10 D. Yang, H. Sasabe, T. Sano and J. Kido, *ACS Energy Lett.*, 2017, **2**, 2021–2025.

11 S.-L. Chang, F.-Y. Cao, W.-C. Huang, P.-K. Huang, K.-H. Huang, C.-S. Hsu and Y.-J. Cheng, *ACS Energy Lett.*, 2018, **3**, 1722–1729.

12 S. M. Tuladhar, M. Azzouzi, F. Delval, J. Yao, A. A. Y. Guilbert, T. Kirchartz, N. F. Montcada, R. Dominguez, F. Langa, E. Palomares and J. Nelson, *ACS Energy Lett.*, 2016, **1**, 302–308.

13 D. Yang, Y. Wang, T. Sano, F. Gao, H. Sasabe and J. Kido, *J. Mater. Chem. A*, 2018, **6**, 13918–13924.